Effect of intrinsic electromagnetic field inside the nanopores of carbonaceous materials on their hydrogen storage behavior

탄소 기반 소재의 나노 기공 내부의 내재적 전자기장이 수소 저장 거동에 미치는 영향

February 2023

Graduate School of Seoul National University
Department of Material Science Engineering

Soon Hyeong So

Effect of intrinsic electromagnetic field inside the nanopores of carbonaceous materials on their hydrogen storage behavior

Advisor : Chong Rae Park

Submitting a Ph.D. Dissertation of Engineering

October 2022

Graduate School of Seoul National University

Material Science Engineering

Soon Hyeong So

Confirming the Ph.D. Dissertation written by
Soon Hyeong So

December 2022

Chair	Jeong-Yun Sun	(Seal)
Vice Chair	Chong Rae Park	(Seal)
Examiner	Taehoon Kim	(Seal)
Examiner	Jong Hun Kang	(Seal)
Examiner	Seung Geol Lee	(Seal)

Abstract

Effect of intrinsic electromagnetic field inside the nanopores of carbonaceous materials on their hydrogen storage behavior

Soon Hyeong So
Department of Material Science and Engineering
The graduate school
Seoul National University

Hydrogen energy is a promising renewable energy and specifically, hydrogen storage is a bottleneck to commercializing hydrogen energy. Researchers have relied on the synthesis of porous materials in physisorption and lowering the H_2 binding energy of hydride materials in chemisorption, all of which have been conducted in a similar manner respectively. However, the development of hydrogen storage materials applicable to onboard system isn't found yet.

To date, the representative governing parameters in the research field of hydrogen storage material are specific surface area and the H_2 binding energy, the binding energy between the adsorbent and H_2 molecule. To investigate their effectiveness, the established working principle and previously reported results were re-examined and the contents including conventional hydrogen storage technology were presented in Chapter 1. Consequently, several outstanding hydrogen storage performance were identified while it couldn't be explained with the governing parameters. In this regard, I noted the phenomenon of eccentric H_2 storage in carbon nanopores with sub-1 nm diameters reported earlier, finding a lack of deep research on the fundamentals of this phenomenon. I formulate a hypothesis of H_2 storage by intrinsic EMF (IEMF) interaction and Chapter 2 provides the results of verification of hypothesis by building slit carbon nanopore and cylindrical carbon nanopore. The key result of this research is that the resultant IEMF by overlapping carbon walls forms inside the carbon nanopore and it forms differently depending on its morphology. Next, I raise questions about how to modulate the IEMF inside the carbon nanopore practically and whether it is correlated to hydrogen storage performance. Therefore, the further research is conducted and the results are presented in Chapter 3 and 4. It is confirmed that IEMF inside the carbon nanopore can be modulated effectively by tuning pore diameter and atomic composition, which are typical methods to control gas adsorption properties. Moreover, it is found that its modulation is highly correlated to hydrogen storage performance, making a breakthrough in designing hydrogen storage materials. This research covers host-guest interaction in addition to the unusual phenomenon occurring in the carbon nanopore with a diameter of sub-1nm and consequently, gives a new insight on other research fields (e.g., supercapacitor, battery, catalyst). On that basis, we successfully synthesize nitrogen plasma-treated N-doped microporous carbon that contains large pore volume below 1 nm and small amount of nitrogen and measure its hydrogen storage performance at room temperature (Chapter 5).

Keyword : hydrogen storage, intrinsic electromagnetic field, carbon nanopore, host-guest interaction

Student Number : 2015-20831

Table of Contents

Part I. General introduction to H_2 storage research

Chapter 1. Introduction.. 2

Part II. Verification of assumption on H_2 storage by intrinsic electromagnetic field (IEMF) interaction

Part III. Development of materials with high performance of H_2 storage by controlling IEMF interaction

Part IV. Conclusions

Part I

General introduction to H_2 storage research

Chapter 1. Introduction

1.1. Importance of the development for hydrogen energy

Global warming is accelerating, which leads to increasing demand to replace fossil fuel with renewable energy. Among various renewable energy, hydrogen energy has been paid attention for the following reasons. First, hydrogen is the most abundant element on Earth while molecular form is present less than 1 percent[1]. The gravimetric energy density of hydrogen (142 MJ/kg) is very high, which is almost 3 times that of LNG gas (47 MJ/kg) and the generation of water during energy production renders energy recycling[1]. The key research on hydrogen energy includes hydrogen production, hydrogen storage, and hydrogen conversion. To commercialize and supply hydrogen energy worldwide, hydrogen storage is the key technology while safety and economic feasibility is required.

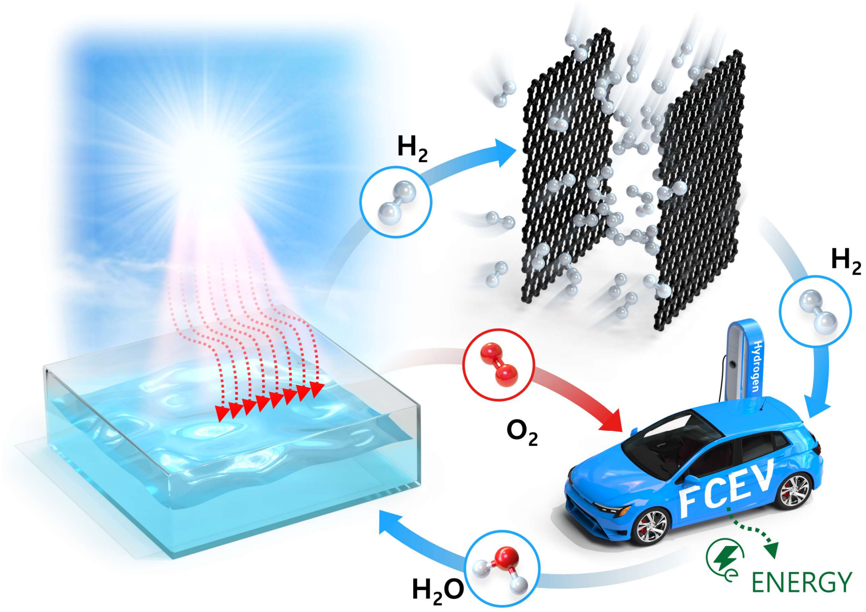

Figure 1.1. Hydrogen energy cycle.

1.2. Conventional methods to store hydrogen

1.2.1. Compression

Hydrogen gas exhibits the very low volumetric energy density of 10.8 kJ/L and to solve this problem, compression into tank at high pressure (350-700 bar) is exploited[2]. Now, most of Fuel Cell Electric Vehicle (FCEC) depend on this technology and this is the best know technology. This technology has the benefits in that the existing LNG gas system can be utilized without building new infrastructure. However, the high-pressure environment is accompanied by safety issue and high cost to manufacture a tank to withstand high pressure.

Figure 1.2. High-pressure tank to compress hydrogen for storage.

1.2.2. Liquefaction

Liquid hydrogen storage is undergoing at 20 K, which is the boiling point of molecular hydrogen, and storage with high volumetric density (70 g/l) and volumetric energy density (8 MJ/l) is possible[2]. However, this technology shows the demerits of evaporation over time and energy loss of 35% during cooling and charging hydrogen in addition to high cost of manufacturing metallic double-walled tank to maintain cryogenic temperature [2].

Figure 1.3. Insulator tank to store hydrogen in liquid form.

1.3. Theoretical background of previous hydrogen storage research

Conventional technology to store hydrogen have innate limitations as mentioned above and to solve this problem, researchers have relied on adsorption phenomenon, which is typically classified as physical adsorption (physisorption) and chemical adsorption (chemisorption).

Physisorption means that the adsorbate is attracted to the surface of adsorbent by van der Waals force, so that the adsorbent is required to have high specific surface area (SSA) and is normally porous material [2]. The strength of interaction is described as the H_2 binding energy and its value of physisorption is nearly 5 kJ/mol, signifying that it is the very weak interaction [3]. To make up this innate limitation, extensive efforts to increase SSA have been made with various porous materials [4,5], however, the research is at a standstill.

Chemisorption is the mechanism that hydrogen molecule is converted into hydrogen atom and it binds to certain sites of adsorbent covalently, ionically, or metallically with the H_2 binding energy exceeding 50 kJ/mol[3]. Chemisorbed hydrogen storage materials include metal hydrides, complex hydrides, and organic molecules, showing high theoretical hydrogen storage performance; however, their typical disadvantages of sluggish kinetics and irreversibility that caused by the strong interaction between hydrogen atom and adsorbent hinder their wide use [3]. To this end, researcher have made efforts to decrease the H_2 binding energy, thereby decreasing the interaction.

In principle, the interaction between the adsorbent and molecular hydrogen can be described with 1-D potential energy curve as a function of the distance between them. Molecular hydrogen can stick to the surface of adsorbent by van der Waals interaction as molecular hydrogen get close to it, which is explained by the shallow well of potential energy. If molecular hydrogen gets close to the surface of adsorbent and the adsorbent fulfill the condition to overcome the activation energy for dissociation of molecular hydrogen and the formation of C-H bond, the chemical reaction undergo, and this is how chemisorption occur. The deep well of potential energy explain the characteristics of chemisorption well.

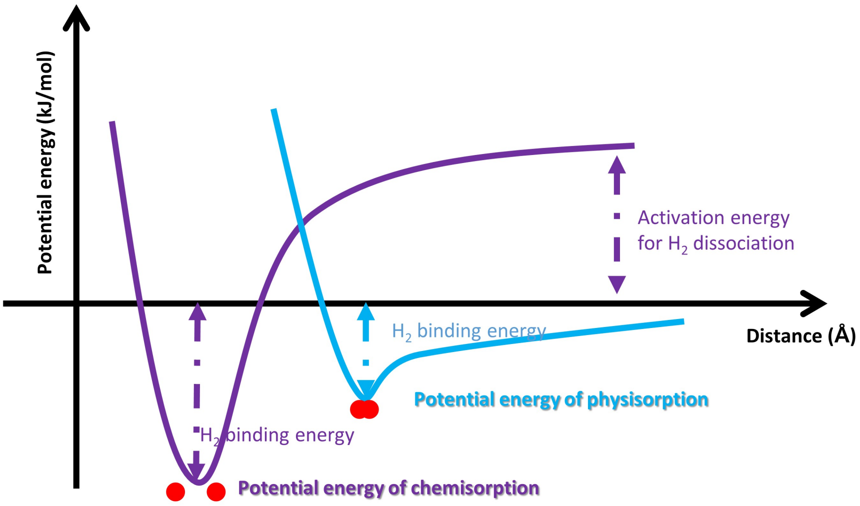

Figure 1.4. 1-D Potential energy curve for describing the interaction between the adsorbent and molecular hydrogen.

1.4. State-of-the-art of hydrogen storage materials and their facing limitations

1.4.1. Physisorption-based storage of molecular hydrogen

Physisorption mainly occurs on the surface of adsorbent, so that increasing SSA expects us to get high H_2 storage performance and a lot of H_2 storage performance of porous materials have been reported[6-9]. Nishihara et al. investigated the gravimetric hydrogen storage capacity (GHSC) of Zeolite-templated carbons (ZTC) at 300 K and 100 bar, showing that ZTC with the largest SSA of 3800 m^2/g exhibit the highest GHSC[10]. Several series of MOF-derived carbon (MDC) were synthesized through thermal treatment under N_2 atmosphere as shown in Figure 1.5.A. MDCs derived from different IRMOFs display SSA outcomes of 3174 m^2/g and 1678 m^2/g with corresponding GHSCSs of 0.94 wt% and 0.60 wt% GHSC at 300 K and 100 bar [6]. Yuan et al. synthesized MOF with different ligands as shown in Figure 1.5.B., and measured the GHSC of MOFs termed PCN-61, PCN-66, and PCN-68 at 300 K and 90 bar. It was found that the GHSC of the isoreticular series of MOF named PCN-61, PCN-66, and PCN-68 are 1.01 wt%, 0.79 wt%, 0.67 wt%, in accordance with the SSA outcomes [11]. Jordá-Beneyto et al. measured the GHSCs of carbon materials at 300 K under high pressure and compared their values to earlier findings [12]. Among their carbon materials, i.e., activated carbons, multiwall carbon nanotube, and carbon nanofibers, their activated carbon KUA5 showed the highest GHSC of 1.2 wt% at 300 K and 200 bar with its large SSA of 3183 m^2/g. The GHSC of KUA6 with a slightly higher SSA was found to be 1.05 wt% under identical conditions. All data about the materials using physisorption mentioned earlier are presented in Table 1.1. and the plot of the GHSC as a function of the SSA is presented in Figure 1.6.

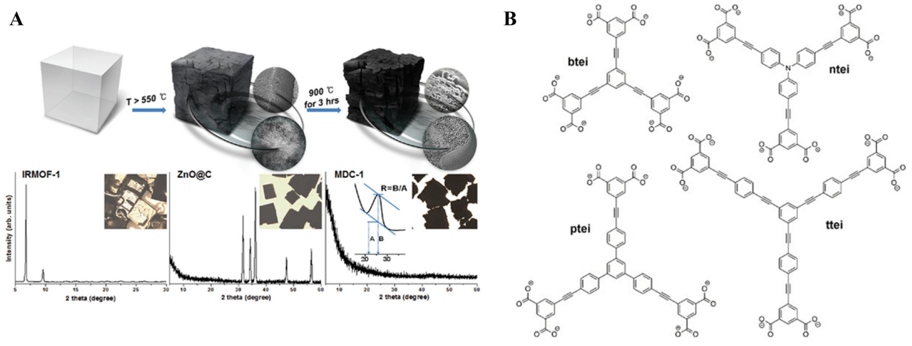

Figure 1.5. Structural change of IRMOF-1 through thermal treatment to synthesize MDC : scheme and Powder X-ray diffraction (XRD) patterns (reproduced with permission[6]. Copyright 2012 ACS Publications), (B) Nanoscopic ligands btei (PCN-61), ntei (PCN-66), and ttei (PCN-610) (Reproduced with permission. Copyright 2010, Wiley-VCH[11])

Table 1.1 : H_2 storage properties of materials with high SSAs

Sample code	GHSC (wt%)	SSA (m^2/g)	Temperature (K)	Pressure (bar)	Ref
P7(2)-H	0.87	3800	300	100	10
MDC-1	0.94	3174	300	100	6
MDC-3	0.60	1678	300	100	
PCN-61	0.67	3000	300	90	11
PCN-66	0.79	4000			
PCN-68	1.01	5109			
KUA5	1.20	3183	300	200	12
KUA6	1.05	3808			
AX21	1.10	2513			

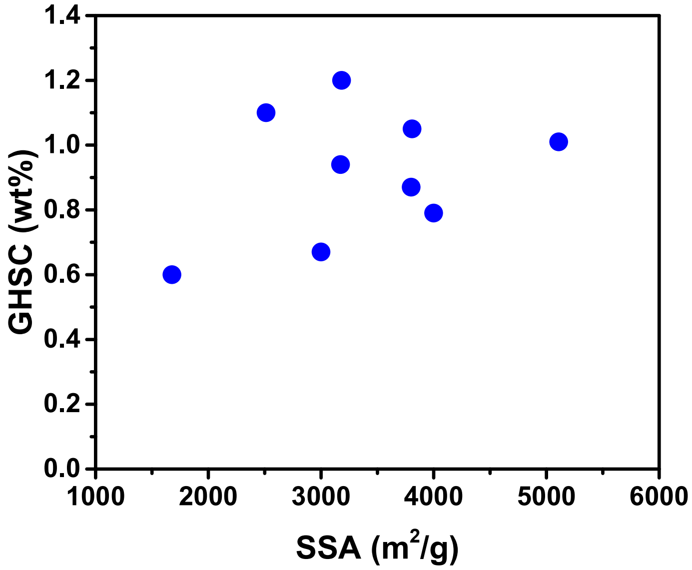

Figure 1.6. GHSC as a function of the SSA in reference to physisorption materials, all of which are mentioned earlier.

1.4.2. Storage of H atom by chemisorption

As shown earlier, storage in the molecule state shows weak interaction with materials, whereas, chemical storage in H atoms is linked to an overly strong interaction between materials and hydrogen molecules. Materials that rely on chemisorption include metal hydrides, complex hydrides, and organic molecules; all of which were mainly developed to realize lower H_2 binding energy levels to release hydrogen readily. Typical metal hydrides take in Lithium hydride (LiH), Sodium hydride (NaH), Magnesium hydride (MgH_2), and Titanium hydride (TiH), and all display high H_2 binding energy levels with substantial GHSCs. Complex hydrides include Lithium aluminum hydride ($LiAlH_4$), Sodium aluminum hydride ($NaAlH_4$), Lithium borohydride ($LiBH_4$), $NaBH_4$, Lithium amide (Li_3N), and NH_3BH_3. Organic molecules for hydrogen storage materials cover Cyclohexane, Methyl-cyclohexane, Decalin, Bicyclohexyl, and Methanol. The GHSC, H_2 binding energy, and dehydrogenation temperature of the materials using chemisorption are presented in Table 1.2.

Table 1.2 : H_2 storage properties of H chemisorbed materials.

Material	GHSC (wt%)	H_2 Binding Energy (kJ/mol)	$T_{dehydro}$ (°C)	Ref
LiH	12.7	233.0	720	[13]
NaH	4.2	113.0	425	
MgH_2	7.6	75.3	327	
TiH_2	4.0	Not mentioned (N.M.)	380	
$LiAlH_4$	8.0	116.0	201	[14]
$NaAlH_4$	5.6	56.5	265	
$LiBH_4$	13.5	52.0-76.0	180-500	
$NaBH_4$	10.8	94.3	400	[13,15]
Li_3N	9.3	80.5	255	[16]
NH_3BH_3	19.6	672	> 500	[17]
Cyclohexane	7.2	68.6	300[a]	[18-20]
Methyl-cyclohexane	6.2	68.3	320[a]	
Decalin (trans)	7.3	66.7	320[a]	
Bicyclohexyl	7.3	66.6	N.M.	
Methanol	12.0	45.5	827	[19,21]

It is found that the overly strong H_2 binding energy hinders the use of these materials as H_2 storage materials under ambient conditions. To overcome this problem, various attempts to decrease the H_2 binding energy have been made in various ways, for example, alloying, the introduction of heteroatoms, and morphological variations.

Alloying is a tool that modifies the H_2 binding energy by introducing metal elements that exhibit different H_2 affinity characteristics. Alloys for hydrogen storage can be classified as AB alloys, AB_2 alloys, AB_5 alloys, and A_2B alloys where solid solution alloys and A and B refer to individual metal elements[22]. Typical alloys are classified as AB [e.g., TiFe, $TiFe_xMn_{(1-x)}$], AB_2 [e.g., $ZrMn_2$], AB_5 [e.g., $LaNi_5$], A_2B [e.g., Mg_2Ni], non-stoichiometric alloy [e.g., $Ti_{0.9}Zr_{0.1}MnCr_{0.9}V_{0.1}$] and solid solution [e.g., $Ti_{0.47}V_{0.46}Mn$]. TiFe is feasible as a hydrogen storage material because it is inexpensive, non-toxic, and abundant. However, it requires a harsh activation process involving high pressures and temperatures (~400 ℃), which cannot readily be exploited in real life[23]. Mn substitution improves the activation process; however, the low GHSC is not improved significantly. The use of a rare earth metal in AB_2 alloys and AB_5 alloys complicates the use of these materials despite the remarkable hydrogen properties. The superior H_2 performance of A_2B alloys has attracted the attention of researchers; however, the high operating temperature and sluggish kinetics are disappointing. Non-stoichiometric alloys consist of many metal elements, leading to low GHSCs. For solid-solution alloys, the fast absorption/desorption under ambient conditions is fascinating, however, the low GHSC is unsatisfactory for on-board vehicular applications. All data regarding the characteristics of metal alloys for H_2 storage are presented in Table 1.3.

Table 1.3 : H_2 storage properties of metal alloys

Material	**GHSC (wt%)**	**H_2 Binding energy (kJ/mol)**	**$T_{dehydro}$ (°C)**	**$P_{dehydro}$ (bar)**	**Ref**
$TiFeH_2$	1.31	28.1	55	10	[24-26]
$TiFe_{0.95}Mn_{0.05}H$	1.30	28.2	55	10	
$TiFe_{0.85}Mn_{0.15}H$	1.63	29.5	55	5	
$ZrMn_2H_2$	1.77	38.0	167	1	[27,28]
$LaNi_5H_6$	1.37	30.9	25	1	[24,27]
Mg_2NiH_4	3.30	64.5	255	1	[24]
$Ti_{0.9}Zr_{0.1}MnCr_{0.9}V_{0.1}H$	0.49	22.5	30	24	[29]
$Ti_{0.47}V_{0.46}MnH_{1.5}$	1.53	25.4	30	120	[30]

The H_2 binding energy of the cycloalkane system can also decrease by the substitution of carbon elements for nitrogen elements[31]. Pez et al. firstly suggested that the partial substitution of carbon atoms into the ring for nitrogen could reduce the aromaticity of the dehydrogenated molecules via a patented concept[19]. For example, N-ethyl carbazole with Pd catalyst is hydrogenated at 160 °C and 72 bar, and dehydrogenation with Ru catalyst occurs at 50-197 °C reversibly without degradation [32]. Cui et al. also showed that the incorporation of heteroatoms in the ring can lower the dehydrogenation enthalpy through a Gaussian calculation[33]. Upon verification with related research, modification of H_2 binding energy is obvious but the innate GHSC is unbetterable. All data about H_2 storage properties of heteroatom-doped organic molecules are presented in Table 1.4.

Table 1.4 : H_2 storage properties of heteroatoms-substituted organic molecules

Material	GHSC (wt%)	H_2 Binding energy (kJ/mol)	Ref
N-isopropyl-carbazole	5.7	49.4	34
N-propyl-carbazole	5.7	50.4	
N-butyl-carbazole	5.4	50.3	
N-ethyl carbazole	5.8	50.6	35
1-ethyl indole	5.8	51.9	

Morphology control can tune both the kinetics and thermodynamics of the H_2 storage behavior in metals. The decreased size with typical methods such as ball milling cannot lead to significant changes in the H_2 binding energy[36]. It has been computationally shown that the crystalline size should be below a critical value to decrease the H_2 binding energy practically, as it leads to an electronic structure on the nanoscale from that on the bulk scale[37]. Therefore, finding a synthesis method for nanoscale materials is important without sacrificing the GHSC. Li et al. synthesized Mg nanowires with various diameters through a vapor-transport method as shown in Figure 1.7A, and demonstrated that thinner Mg/MgH_2 shows a much lower H_2 binding energy of 65.3 kJ/mol compared to that of bulk MgH_2 (74 kJ/mol). It is also demonstrated that thinner Mg nanowires display easier activation for hydrogen absorption/desorption. However, the nanowire morphology is not retained upon cycle testing and a high temperature (573 K) is still required to attain the proper GHSC (7.6 wt%) outcome as shown in Figure 1.7B[38]. Zhang et al. synthesized ultrafine MgH_2 and reported remarkable H_2 storage performance of 6.7 wt% at 300 K and 30 bar with the H_2 binding energy of 59.5 kJ/mol, though the required absorption time was 6 h. At 85 ℃, 6.3 wt% was achieved within 25 min and full hydrogenation (6.7 wt%) was completed within 60 min. It should be noted that this marked the first time to show the reversibility of an MgH_2-based material under ambient conditions. This result indicates that optimal morphology control has the potential method to pave the way for the development of viable H_2 storage materials[39]. The data mentioned in this paragraph are presented in Table 1.5 and the plot of the GHSC as a function of the H_2 binding energy for materials using chemisorption is presented in Figure 1.8.

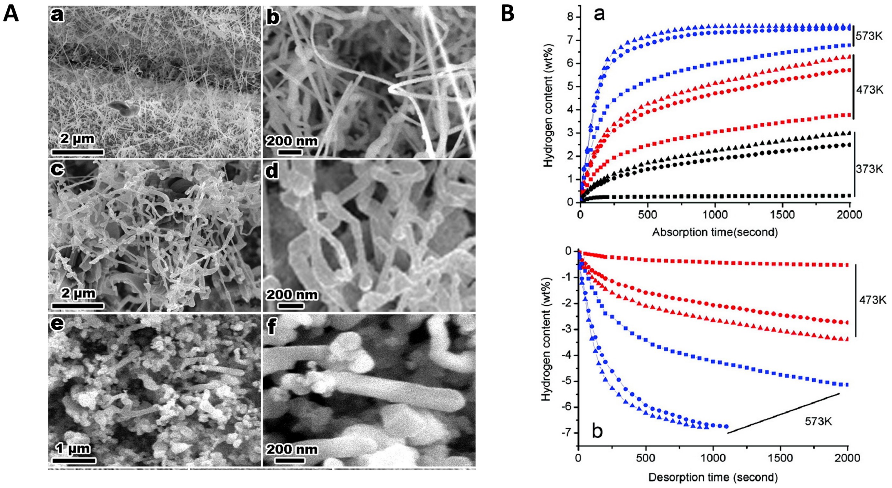

Figure 1.7. (A) SEM images of Mg nanowires: sample 1 (a, b), sample 2 (c, d), sample 3 (e, f) (B) Hydrogen absorption (a) and desorption (b) of the Mg nanowires (sample 1: triangle, sample 2: circle, sample 3: square). The sample code is named with different diameters of Mg nanowires (sample 1: 30-50 nm, sample 2: 80-100 nm, sample 3: 150-170 nm). Reprinted with permission[38]. Copyright 2007 ACS publications.

Table 1.5 : H_2 storage properties of morphology-controlled-Mg

Sample code	**GHSC (wt%)**	**H_2 Binding energy (kJ/mol)**	**Morphology**	**$T_{dehydro}$ (°C)**	**$P_{dehydro}$ (bar)**	**Ref**
Sample 1	7.6	65.3	Nanowire	300	0.2	38
Non-confined ultrafine Mg nanoparticles	6.7	59.5	Nanoparticle	80	$3.8 * 10^{-3}$	39

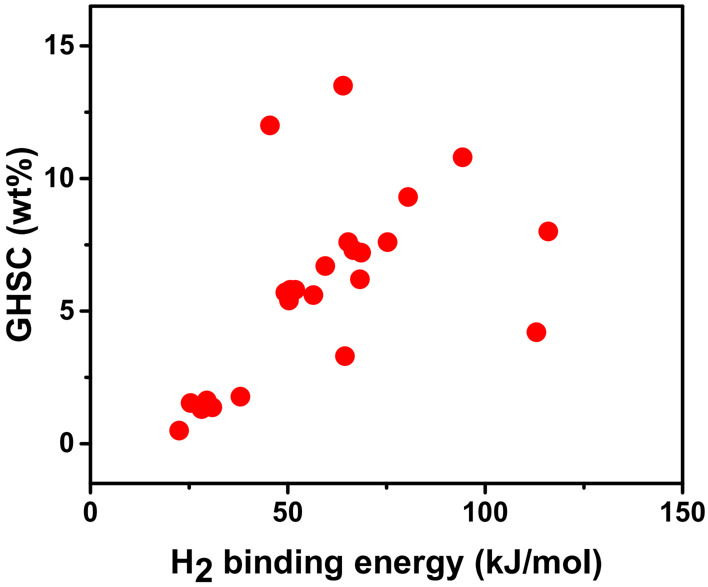

Figure 1.8. Scatter plot of the correlation between the GHSC and H_2 binding energy in reference to chemisorption-based materials, all of which were mentioned previously here.

1.4.3. Modulation of the H_2 binding energy by various strategies

When using physisorption, the strategies to increase SSA and GHSC are considered to have reached the limit of technology and are now displaying a tendency towards GHSC saturation (Figure 1.6.). On the other hand, efforts to decrease the H_2 binding energy in chemisorption have shown a weak correlation between the GHSC and H_2 binding energy as shown in Figure 1.8.; in addition, the innate characteristics of slow kinetics and poor reversibility make practicality difficult. To realize a breakthrough, efforts to increase the H_2 binding energy in physisorption have been made and orbital interactions with the H_2 binding energy that are known to lie between physisorption and chemisorption have been exploited.

1.4.3.1. By increasing the H_2 binding energy (10.0-21.7 kJ/mol) with the introduction of heteroatoms into porous materials

It has been suggested that the introduction of heteroatoms with different electronegativity properties, for example, boron, nitrogen, oxygen, or lithium inside nanomaterials can increase the H_2 binding energy by localizing electrons. As a representative of this approach, nitrogen doping effects on hydrogen storage have widely been studied experimentally and computationally[40-44]. Jiang et al. reported outstanding performance of 2.21 wt% at 300 K and 80 bar and 0.98 wt% at 77 K and 1 bar with a hollow nitrogen-containing carbon sphere, referred to as MCN-1-3 h in their study. The material contains 2.3 wt% N content, 872 m^2/g SSA, and 0.49 cm^3/g micropores by volume. The author explained that uniformly sized micropores and a large pore volume facilitate physisorption and that the nitrogen in the carbon framework activates the hydrogen molecules, which together increase the H_2 binding energy (up to 22 kJ/mol). In consequence, the H_2 storage performance is enhanced. However, the preparation of B-doped carbon with a high B content is not relatively easy in the case of N-doped carbon. Chung et al. synthesized microporous boron-substituted carbon materials using polymeric precursors, and the material (BC-II-800) with the highest level of B contents (7.2 wt%) and SSA (780 m^2/g) displayed the highest H_2 storage performance of 0.4 wt% at 300 K and 56 bar and 1.6 wt% at 77 K and 1 bar[45]. Considering the value of SSA and comparing the GHSCs of carbon nanomaterials, the stored H_2 quantity must be thought to be high and it was reported that the high performance is attributed to the high H_2 binding energy (~11 kJ/mol) induced by the introduction of boron atom. Jeong et al. fabricated 12% B-containing porous carbon and showed a significant B doping effect on the enhancement of the H_2 storage performance. Notably, BC_6 exhibits high H_2 binding energy of 20 kJ/mol[46]. Moreover, the researchers insisted that N or B doping decreases the activation energy of H_2 dissociation such that this approach could be effective for hydrogen dissociation and storage[47]. On the other hand, the oxygen doping effect on hydrogen storage is quite controversial[48-50]. Nevertheless, it was reported that AC created through the hydrothermal carbonization of cellulose acetate exhibit a tremendous SSA value (up to 3771 m^2/g), representing the champion value for AC and CA-4700, one of their samples, stores hydrogen molecules, 0.8 wt% at 300 K and 30 bar and 8.9 wt% 77 K and 30 bar. They clarified that the oxygen-rich nature leads to high H_2 binding energy (10 kJ/mol), compared to that of zeolite-template carbon (8 kJ/mol)[51]. All data regarding H_2 storage properties of heteroatoms-doped porous materials are presented in Table 1.6.

Table 1.6 : H_2 storage performance of heteroatoms-embedded porous materials

Sample code	GHSC (wt%)	H_2 Binding energy (kJ/mol)	SSA (m^2/g)	Temp (K) / Pressure (bar)	Ref
MCN-1-3h	2.21	21.7	872	300 / 80	[52]
BC-II-800	0.40	11.0	780	300 / 56	[45]
BC11	0.37	12.5	780	293 / 80	[46]
BC6	0.54	20.0	609	293 / 80	[46]
CA-4700	0.80	10.0	3771	300 / 30	[51]

Furthermore, boron nitride was suggested to maximize these effects and some researchers found computationally that the H_2 binding energy of boron nitride is higher than that of graphene, indicating that boron nitride is a promising candidate for hydrogen storage[53,54]. It is thought by some researchers that boron nitride can be utilized with both physisorption and chemisorption. Ma et al. synthesized two types of BN nanotubes through a chemical vapor deposition process by pyrolyzing the B-N-O precursor at ~2000 K under an N_2/NH_3 atmosphere. It was noted that varying the oxygen content results in different morphologies of BN nanotubes, specifically multiwall BN nanotubes and bamboo BN nanotubes. Despite a lack of information about the SSA, this method must show high performance and it is inferred that the main mechanism is chemisorption because the majority (70%) of H_2 is retained after depressurizing and the equilibrium time at each pressure reaches 4 hours[55]. Reddy et al. also reported similar results by controlling the morphology of boron nitride[56]. It was found that variation of the growth temperature from 1000 to 1150 °C under an NH_3 gas flow leads to variations in the morphology (e.g., flower, short bamboo, long bamboo, and straight wall) with each displaying different H_2 storage performance. The highest H_2 storage performance among the samples is displayed in the long bamboo BN case, and it shows a considerably high GHSC (3.0 wt% at 300 K and 100 bar) despite the low SSA (230 m^2/g). Li et al. asserted that boron nitride with a whisker morphology exhibits a superior GHSC of 5.6 wt% at 300 K and 30 bar, representing the world record for boron nitride to the best of our knowledge, even under moderate pressure. The cause of the high performance is attributed to the large micropore volume (0.45 cm^3/g), high SSA (1687 m^2/g), and B-N polar bonds[57]. In addition, BN hollow spheres (BNHSs) with ultrathin shells (1-3 nm) were developed, and among them, BNHSs C reaches a level of 4.07 wt% H_2 uptake at 300 K and 100 bar with a low SSA (215 m^2/g). More interestingly, a second adsorption outcome of 3.93 wt% at 300 K and 100 bar is confirmed with hydrogen adsorption against the SSA showing a world-record value to the best of our knowledge for BN nanomaterials. It is said that the outstanding performance is due to the large SSA, a large number of micropores, B-N bonding on the bent surface, and the high density of structural defects[58]. Overall, boron nitride appears to be a ground-breaking material for hydrogen storage; however, no fundamental study exists to look into the correlation between the composition and H_2 binding energy. Rather, existing parameters such as the number of micropores, the SSA, and the morphology are reused to explain the high H_2 storage performance. All data about H_2 storage properties of boron nitride are presented in Table 1.7.

Table 1.7 : H_2 storage performance of boron nitride

Sample code	**GHSC (wt%)**	**H_2 Binding energy (kJ/mol)**	**Morphology**	**Temp (K) / Pressure (bar)**	**SSA (m^2/g)**	**Ref**
Multi-wall tube	1.8	N.M.	Multiwall	300 / 100	N.M.	55
Bamboo tube	2.6	N.M.	Bamboo	300 / 100	N.M.	
Bamboo-type BN	3.0	N.M.	Long bamboo	300 / 100	230	56
HBBN-1	5.6	N.M.	Whiskers	300 / 30	1687	57
BNHSs C	4.1	N.M.	Hollow sphere	300 / 100	215	58

Simultaneous hydridic and protonic H atom storage is possible with Frustrated Lewis Pairs (FLP). The FLP is a compound containing a Lewis acid and a Lewis base. Lewis bases/acids are materials that donate/accept electrons to/from other species and in general, tend to be united for neutralization. However, they cannot be bonded due to the steric hindrance of the surrounding bulky groups. Typical examples of FLPs are intermolecular or intramolecular combinations of bulky phosphines or amines with strongly electrophilic $RB(C_6F_5)_2$ components[59]. Therefore, it is said that the exposure of H_2 to a FLP generates salts due to the heterolytic cleavage of H_2 molecules. Some researchers have modified bulky groups for reversibility at low temperatures and have shown increasing GHSC levels[59-63]. Welch et al. reported that the compound $(C_6H_2Me_3)_2PH(C_6F_4)BH(C_6F_5)_2$ (Me : methyl) is derived from a reaction involving dimesitylphosphine substitution at the para carbon of tris(pentafluorophenyl) borane with dehydrogenation occurring near 373 K. In addition, the dehydrogenated form is stable and reverts to the parent form at 300 K and 1 bar H_2[64]. Unfortunately, the GHSC is less than 0.25 wt% despite its suitable operating condition for onboard hydrogen storage. Thus, it is inferred that it would be better to serve as a metal-free catalyst for hydrogenation due to the heavy bulky group.

1.4.3.2. By increasing the H_2 binding energy (6.1 ~ 21.0 kJ/mol) via coordinatively unsaturated metal sites of MOFs

MOFs have attracted attention as a new class of gas storage materials with low density and high SSA levels. They consist of inorganic clusters bound to an organic linker, forming a strong bond, such that they are robust and stable materials under dry conditions. Various inorganic clusters and organic linkers have been combined and the H_2 storage performance of these materials was measured. While no breakthrough was observed, researchers discovered that in some types of MOFs, the formation of an open metal site to increase the H_2 binding energy is feasible by removing coordinated molecules via heating or evacuation[65]. For example, Dinca et al. reported the H_2 storage performance of Mn-BTT (BTT^{3-} = 1,3,5-benzenetristetrazolate), which is fabricated by solvent exchange from $[Mn(DMF)_6]_3[(Mn_4Cl)_3(BTT)_8(H_2O)_{12}]_2\cdot 42DMF\cdot 11H_2O\cdot 20CH_3OH$ to $[Mn(CH_3OH)_6]_3[(Mn_4Cl)_3(BTT)_8(CH_3OH)_{12}]_2\cdot 42CH_3OH$, and subsequently to $Mn_3[(Mn_4Cl)_3(BTT)_8(CH_3OH)_{10}]_2$ with evacuation. To prove the correlation between the exposed Mn^{2+} site and the high H_2 binding energy, neutron diffraction experiments were conducted and the possible sites of H_2 binding were suggested. It was insisted that a key concept of hydrogen storage research is the ability to control the H_2 binding energy and that increasing the H_2 binding energy should be accomplished for H_2 storage under ambient conditions[66]. Latroche et al.[9] noted that MIL-101, $Cr_3F(H_2O)_2O[C_6H_4(CO_2)_2]_3$, provides unsaturated chromium sites after the removal of terminal water molecules and that these may explain the H_2 performance and H_2 binding energy (~10 kJ/mol). Given the H_2 binding energy reported for MOFs in the range of 4 to 7 kJ/mol, these are thought of remarkable results, however, the positive effect is squashed by the heavy weight of the metal for high H_2 storage performance at RT. Nonetheless, some reported plain H_2 binding energy outcomes despite the open metal sites[11,67]. Jaramillo et al. synthesized $V_2Cl_{2.8}$(btdd) with an exposed V site, finding that the H_2 binding energy of the material reaches 21 kJ/mol, with the interaction between the material and the H_2 molecules characterized by powder neutron diffraction, in-situ infrared data, and Density-functional-theory (DFT) calculation. The charge transfer between V and H_2 molecules and H_2 polarization was confirmed and high SSA values were calculated. All data about the MOFs with open metal sites are presented in Table 9.

Table 1.8 : H_2 storage performance of MOF with exposed metal site

Sample code	**H_2 Binding energy (kJ/mol)**	**GHSC (wt%)**	**SSA (m^2/g)**	**Temp (K) / Pressure (bar)**	**Ref**
Mn-BTT	10.1	0.94	2100	300 / 90	66
MIL-101	10.0	0.43	5800	300 / 80	9
SNU-21H	6.1	0.18	695	300 / 70	67
SNU-21S	6.7	0.26	905	300 / 70	
PCN-61	6.4	0.67	3000	300 / 90	11
PCN-66	6.2	0.79	4000	300 / 90	
PCN-68	6.1	1.01	5109	300 / 90	
$V_2Cl_{2.8}$(btdd)[a]	21.0	0.80	1920	300 / 100	68

[a] bis(1H-1,2,3-triazolo[4,5-b],[4′,5′-i])dibenzo[1,4]dioxin

1.4.3.3. By increasing the H_2 binding energy (5.3 ~ 13.3 kJ/mol) via the effect of H_2 nanoconfinement in the nanopore of sub-1 nm

Nanopore with a diameter of sub-1 nm can interact with H_2 molecules stronger than does on an open flat surface by overlapping the potential from opposite walls[1]. Related research has been reported for ages both computationally and experimentally[69-72]. Patchkovskii et al. showed that the H_2 binding energy increase as the interlayer distance of bilayer graphene decrease by conducting theoretical studies on the bilayer graphene-H_2 system. Gallego et al.[69] confirmed the advantages of adsorption-storage over compression-storage by investigating H_2 density confined in activated carbon at room temperature with In-situ small-angle neutron scattering. It was seen that the density of H_2 in nanopore with the diameter of 9 Å at 200 bar is comparable to that of liquid hydrogen as show in Figure 1.9A. Liu et al. recently reported a hydrogen storage material, hydrofluoric acid incompletely etched MXene (Ti_2CT_x)[73]. It displays a GHSC of 8.8 wt% at 300 K and 60 bar despite the very low SSA of 3.3 m^2/g and retains nearly 4 wt% after degassing to 1 bar. The authors insist that so-called nano pump-effect-assisted weak chemisorption in the sub-nanoscale interlayer space induces high H_2 storage performance, presenting the XRD pattern of Ti_2CT_x to reveal an interlayer distance of 6.8-8.7 Å. In addition, the material was tested for thermal stability, reversibility, cyclability, and kinetics, which are essential characteristics for commercialization. To the best of our knowledge, this is a world-record outcome for H_2 storage performance at RT, though leaving doubt about the unexceptional H_2 binding energy of nearly 13 kJ/mol. Besides a lot of researchers have reported the results regarding H_2 nanoconfinement without mentioning the H_2 binding energy. Experimental and theoretical value of variation in the H_2 binding energy with the pore size is presented in Table 1.9.

Table 1.9 : The H_2 binding energy in accordance with pore size

Pore size (Å)	H_2 binding energy (kJ/mol)	Ref
6	13.1	72
7	10.8	
8	8.1	
9	6.7	
10	6.0	
12	5.3	
7	13.3	73

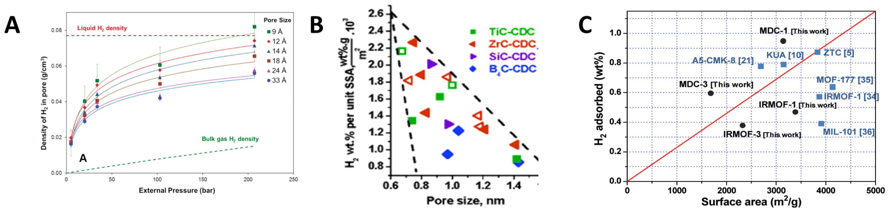

Figure 1.9. (A) Room-temperature densities of adsorbed H_2 as functions of pressure for selected pore sizes. The figure is reproduced with permission. Copyright 2011, ACS publications[69]. (B) Effect of the pore size on the GHSC per unit SSA. The general trend indicates that small pores are more efficient than large pores for a given SSA (Reprinted with permission[74], Copyright 2005, American Chemical Society). (C) GHSC outcomes at 300 K and 100 bar for various types of porous carbon and MOFs plotted as a

function of the SSA. The figure is reproduced with permission. Copyright 2012, ACS publications[6].

Gogotsi et al confirmed the effect of the pore size on GHSC at a given SSA, indicating that a smaller pore size leads to higher GHSC at the given SSA as shown in Figure 1.9B[74]. Jordá-Beneyto et al. measured the GHSC of several microporous materials at 77 K and 300 K and demonstrated that micropores do play an important role in the GHSC at 300 K irrespective of pressure and 77 K under moderate pressure [12]. Cabria et al. presented a computational model of carbon slits with consideration of the quantum effects of the molecules in the confining potential of slit pores[75]. In a graphene bilayer slit pore model, outcomes of 3.2 wt% (6 Å), 2.8 wt% (7 Å), 2.4 wt% (8 Å), 2.1 wt% (9 Å), and 2.0 wt% (10 Å) at 300 K and 100 bar were obtained. Furthermore, it was claimed that the GHSC is strongly dependent on ultrafine micropores (< 0.8 nm) rather than micropores (< 2 nm) with this also indicating that narrow pores play an important role in H_2 storage[76]. MDC with a large micropore volume (1.01 cm^3/g) displayed almost 1 wt% GHSC at 300 K and 100 bar, which is considered to be high H_2 storage performance under ambient conditions, given the SSA of 3174 m^2/g (Figure 1.9C)[6]. Kim et al. reported the GHSC (0.5 wt%) of thermally modulated graphene oxide at 300 K and 90 bar, finding that the optimum interlayer distance (6.5 Å) arises when using the remained oxygen functional group as a spacer after a thermal treatment[77].

1.4.3.4. By modulating the H_2 binding energy (0.5 ~ 50.2 kJ/mol) via exploiting the orbital interaction between H_2 molecules and adsorbents

It is known that transition metal (TM) atoms bind to H_2 molecules through the hybridization of d orbitals and H_2 σ and σ^* orbitals. This interaction is known as the Kubas interaction and the H_2 binding energy ranges from 20 to 40 kJ/mol, which is suggested as the optimal range for vehicular applications[78]. A lot of researchers have studied Kubas-type materials in the viewpoint of hydrogen storage materials theoretically and experimentally[78-84]. Hoang et al. reported that V-Oxamide 150, a sample of tris(mesityl) (Mes) vanadium (III)-THF with oxamide, displays an outcome of 3.49 H_2 wt% at 77 K and 85 bar. Moreover, oxalic acid, glycolic acid, and glycolamide were also chosen to synthesize a series of 1 D V(III) polymers with trismesityl (Mes) vanadium (III)-THF[81]. In this paper, a GHSC outcome of 0.87 wt% at 300 K and 85 bar is reported as well with H_2 binding energy of 17.9 kJ/mol; this represents a nearly unbelievable result when considering that the SSA of this material is only 9 m^2/g even though that its performance is close to that of MDC, of which the SSA exceeds 3000 m^2/g[6]. It was found that 3.5 hydrogen molecules at 77 K and 0.88 hydrogen molecules at 300 K are bound to a vanadium atom based on thermogravimetric results. The phenomenon of an increasing trend of the H_2 binding energy with the GHSC was confirmed by using the Clausius-Clapeyron equation, indicating extraordinary characteristics of Kubas-type materials. The authors designed manganese (II) hydrazide gels for a Kubas-type hydrogen storage material from bis(trimethylsiylmethyl) manganese and anhydrous hydrazine. It was found that the best H_2 storage performance under ambient conditions is 1.06 wt% at 85 bar with their B100 sample; the GHSC outcome under a cryogenic condition is 1.31 wt% at 85 bar without saturation. It was also calculated that the SSA of B100 is 279 m^2/g and that the number of H_2 molecules per manganese atom at 77 K and 300 K is 0.58 and 0.47 respectively[83]. Hamaed et al. used low coordinate Ti (III) fragments, 0.2TiBz$_4$-HMS with a SSA of 1294 m^2/g, demonstrating that the GHSC of this material is 1.66 wt% at 77 K and 60 bar and 0.69 wt% 300 K and 60 bar[85]. The authors also showed high and reversible H_2 storage performance of 3.23 wt% at 300 K and 170 bar with their chromium hydrazide gel, H2-Cr-MHz (1.5). The GHSCs of H2-Cr-MHz (0.5) and H2-Cr-MHz (1.0) at 300 K and 85 bar were measured as well as 1.41 wt% and 1.65 wt% respectively, which are excellent performances under ambient conditions[82]. Morris et al. prepared vanadium (III) alkyl hydrides from a vanadium (III) alkyl complex, showing that this material exhibits an outcome of 5.4 wt% reversibly at 300 K and 120 bar, close to the DOE target for 2020. This is the first time that saturation is observed in an H_2 isotherm of a Kubas-type material. It was found that the material falls between the VH_5 and VH_7 phase by calculating the capacities and that Kubas interaction may pave the way for a breakthrough in the H_2 storage material field given the SSA of 3

m^2/g. H_2 binding energy (endothermic 0.52 kJ/mol) was measured by the calorimetry method and was attributed to structural deformation that buffers the H_2 binding energy of 30-50 kJ/mol expected for Kubas binding while preventing saturation of the isotherm. With high-pressure Raman spectroscopy, it was found that 2770, 2929, and 3834 cm^{-1} appear when purging H_2 with these corresponding to three different Kubas binding sites[86]. Unfortunately, the Kubas-type material tends to be oxidized or aggregated. Therefore, a materialization of the targeted structure is highly challenging such that it may not be viable for commercialization as yet[87]. The data about H_2 storage properties of Kubas-type materials are presented in Table 1.10.

Table 1.10 : H_2 storage performance of Kubas-type materials

Material	**H_2 Binding energy (kJ/mol)**	**GHSC (wt%)**	**SSA (m^2/g)**	**Temp (K) / Pressure (bar)**	**Ref**
V(III) polymer	17.9	0.87	9	300 / 85	[81]
Mn hydrazide gel	25.0	1.06	279	300 / 85	[83]
Ti(III) fragments	22.0	0.69	1294	300 / 60	[85]
Cr hydrazide gel	50.2	1.65	171	300 / 85	[82]
V(III) alkyl hydride	0.5	5.40	3	300 / 120	[86]

Hydrogen spillover was initially observed by Khoobiar in 1964, in which yellow WO_3 was reduced to blue WO_{3-x} with Pt catalyst and hydrogen gas[88]. This is a well-known phenomenon in the catalysis field, and its mechanism remains under study[89]. Yang's research group as a representative has long studied hydrogen storage by spillover and many related papers have been published[7,90-99]. In general, a metal catalyst such as Pt, Pd, or Ni is introduced onto a porous material. It was suggested that when hydrogen gas is injected, atomic hydrogen dissociated by the metal catalyst migrates from the metal catalyst to the porous material with this process possibly occurring reversibly from the support material to the metal catalyst when the hydrogen gas is depressurized[100]. Li et al. [93] studied the equilibrium and kinetics of hydrogen storage on Pt-doped Activated carbon (Pt/AC) where the material was synthesized by an impregnation method using ultrasonication. The Pt/AC displayed an outcome of 1.2 H_2 wt% at 300 K and 100 bar with an enhancement factor of 2 and a H_2 binding energy of 23 kJ/mol. It was found that at low pressure (80 Torr), H_2 adsorption is rapid, taking less than 10 sec to reach equilibrium; the activation energy of hydrogen surface diffusion is 7.6 kJ/mol, and the diffusion time constant decreases with an increase in the pressure. It was also noted that the average diffusion distance increased with pressure (surface concentration). Wang et al.[44] found a 2.4-fold enhancement of GHSC by spillover, with Pt supported on N-doped C showing GHSC of 1.26 wt% at 300 K and 100 bar and high H_2 binding energy (30 kJ/mol), an outcome higher than that of N-doped C (7.3 kJ/mol). They synthesized Ru-doped Templated Carbon (TC), Pt-doped TC, and Ni-doped TC and confirmed that the maximum GHSC at 300 K and 100 bar is 1.43 wt% on Ru/TC with an enhancement factor of 1.8. All samples display a similar range of H_2 binding energy, and it decreases with the adsorbed amount[91]. Li et al. insisted that very close contact between the catalyst and the receptor material is important to decrease the energy barrier for hydrogen diffusion, also reporting that a carbon bridge made from sucrose enhances the GHSC from 0.5 wt% for pristine IRMOF-8 to 4.0 wt% for the Pt/AC-bridges-IRMOF-8 at RT and 100 bar. It was also noted that the second adsorption is in agreement with the first adsorption and the H_2 binding energy ranges from 20 to 23 kJ/mol[101]. Despite these interesting results, some researchers have opposed the results flatly. Campesi et al. revisited the Pt/AC+IRMOF 1+sucrose system studied by Li et al. and measured the GHSC of Pt/AC, IRMOF-1, an unbridged sample, and a bridged sample at 300 K and 100 bar. It was asserted that no enhancement of the GHSC was found, whereas a slight decrease in the GHSC was uncovered[102]. Stadie et al. also revisited the Pt/AC system and claimed that Pt particles are detrimental to the GHSC because they increase the weight of the adsorbent, thereby decreasing the SSA with the amount of chemisorbed H on the surface of Pt being negligible[103]. And Oh et al. asserted that no connection between the spillover effect and a meaningful enhancement of GHSC, showing negligible enhancement of GHSC of a Pt-doped TC[104]. That is to say, there is no consensus about H_2 storage performance results with spillover mechanism, meaning that a careful approach is required. The characteristics of H_2 storage materials using the orbital interaction are presented in Table 1.11.

Table 1.11 : H_2 storage performance of transition-metal embedded porous materials using the spillover phenomenon

Material	H_2 Binding energy (kJ/mol)	GHSC (wt%)	SSA (m^2/g)	Temp (K) / Pressure (bar)	Ref
Pt+AX21	23	1.2	2518	300 / 100	[93]
Pt+N doped C	30	1.3	1388	300 / 100	[44]
Ru + Templated C	25	1.4	3004	300 / 100	[91]
Pt/AC+IRMOF8 +sucrose	23	4.0	466	300 / 100	[101]

1.4.4. Insights into future research strategy for the development to make a breakthrough in the field of hydrogen storage

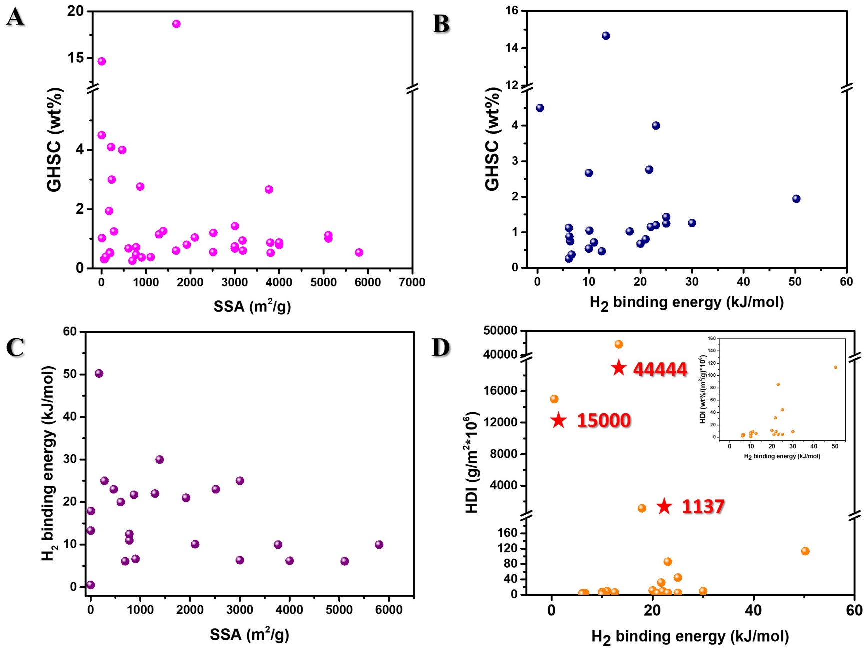

Figure 1.10. Correlation between the GHSC and SSA (A), GHSCs of materials with modified H_2 binding energy vs. the H_2 binding energy (B), the relationship between the H_2 binding energy and the SSA (C), and the H_2 densification index (HDI: $\frac{GHSC}{SSA} * 10^4$) of materials with modified H_2 binding energy as a function of the H_2 binding energy. Inset: the same plot without three superior results (D). All GHSCs measured under different pressure ranges are fitted to the estimated value at 100 bar on the assumption that the GHSC is linear to the pressure.

Both the SSA and H_2 binding energy are thus far representative parameters when evaluating the GHSC; accordingly, the correlation between the GHSC and the SSA (H_2 binding energy) is investigated as shown in Figure 1.10A (Figure 1.10B). All data mentioned in this paper are used. As a result, no correlation between the parameters was found and no relationship between the H_2 binding energy and SSA could be found (Figure 1.10C). The GHSC is influenced not only by how strongly H_2 molecules and the adsorbent interact but also by how many adsorption sites exist on the surface of the adsorbent. In this regard, HDI is obtained to rule out the effect of SSA on the H_2 storage performance and to observe the H_2 storage performance from the perspective of the H_2-adsorbent interaction alone. It is calculated by dividing the GHSC*10^4 by the SSA. HDI versus the H_2 binding energy is plotted as shown in Figure 1.10D where three superior results are shown and the inset in Figure 1.10D displays the same plot without the superior results to keep the superior results from overriding other results. It is noted that the H_2 storage material with the highest HDI (44444) displays the H_2 binding energy below 20 kJ/mol, which is outside the targeted H_2 binding energy range. The second highest HDI (15000) is linked to the H_2 binding energy near 0 kJ/mol. Moreover, no correlation between HDI and the H_2 binding energy is found. This signifies that the H_2 binding energy cannot describe the H_2-adsorbent interaction thoroughly. I think that this is because the H_2 binding energy doesn’t include the concept of space where hydrogen molecules are stored while it is calculated from the one-point minimum value of potential energy of the H_2-adsorbent system. To study the H_2-adsorbent interaction, I noted the phenomena of abnormally dense hydrogen storage in carbon nanopores of sub- 1 nm that are reported earlier[69,70,75], and raised critical questions about the phenomena : (a) What would induce the spontaneous inflow of H_2 molecules into sub-1 nm carbon nanopore, all of which are seemingly neutral in charge?, (b) How could the H_2 molecules introduced into the carbon nanopores be confined and condensed so as to have liquid- or solid-like densities? I noted studies of the structural phase transitions in materials under an external electric field or magnetic field[105-109] and surmised that this may be related to the phase transition of H_2 molecules confined into the carbon nanopores, which deviates from the phase diagram of molecular hydrogen. Taken together, I formulated a hypothesis of hydrogen storage by IEMF interactions, with IEMF referring to an electromagnetic field formed by a material itself without an external energy source.

1.5. Scope and aim of present work

To solve the status of hydrogen storage materials research field, I investigated the underling underlying mechanism of phenomena reported earlier, thereby using it as a stepping stone to find out the correlation between IEMF and H_2 storage performance and to develop hydrogen storage material with high-performance.

Chapter 2 provides the detailed research on the abnormal phenomenon, verifying a hypothesis of hydrogen storage by IEMF interaction. The contents include the presence of an IEMF near a carbon nanopore with a diameter below 1 nm, the type of the interaction between the IEMF from the carbon nanopore and H_2 molecules, the effectiveness of the interaction, and the relationship between the IEMF and the H_2 storage behavior in the carbon nanopores.

Typically, the adsorption properties of materials are controlled by controlling pore size and introducing hetero-atoms. From this fact, I surmise that the IEMF of material can be controlled by the means and whether their modulation effect is effective or not is studied in chapter 3. Furthermore, the correlation between H_2 storage performance and modulated IEMF is examined in Chapter 4.

Morphology and atomic composition are effective methods to modulate IEMF, so that I develop hydrogen storage material, maximizing hydrogen storage by adjusting pore size and N content of the material.

Part II

Verification of assumption on H_2 storage by IEMF interaction

Chapter 2. Identification of the correlation of IEMF interaction and abnormal H_2 storage in carbon nanopores with sub-1 nm diameters.

2.1. Introduction

Hydrogen energy has attracted much attention due to its potential to replace fossil fuels, which inevitably emit CO_2 and cause global climate change. Indeed, hydrogen has a high specific energy of 142 MJ/kg and offers the advantages of natural abundance, no emission of harmful byproducts in the process of gaining energy, and renewability [1]. When utilizing hydrogen energy in practice, particularly in the car industry, there are major hurdles that must be overcome, such as how to store as much the hydrogen gas as possible and how to use it safely at room temperature or the vehicle operation temperature.

Conventionally, hydrogen gas is stored either in a cylindrical tank with the compression pressure of 350-700 bar or in a liquefied form in the cryogenic temperature range (20 K)[110]. However, the boil-off issue caused by heat leaks limits the wider practical application of conventional methods[111]. Alternative routes to more practical and safe hydrogen storage methods include the development of the storage materials based on either the physisorption of H_2 molecules or the chemisorption of H elements[112]. It is generally understood that the merits of physisorption are the fast adsorption/desorption kinetics, good reversibility, and the ambient operating condition, whereas a disadvantage is the weak binding energy between H_2 molecules and the adsorbent, which eventually leads to low gravimetric H_2 storage capacity (GHSC). Much effort has thus been expended to create as many nanopores as possible to store H_2 molecules by developing porous materials such as nano-porous carbons[113], metal-organic-frameworks (MOFs)[8,65,114-116], and covalent-organic-frameworks (COFs)[117-119] with a specific surface area (SSA) as high as possible together with efforts to increase the binding energy of H_2 molecules to adsorbents[120]. However, it is accepted that the GHSC does not increase linearly with an increment of the SSA or with greater H_2 binding energy[3,121,122]. On the other hand, for chemisorption, a high amount of hydrogen can be stored via covalent bonding to either metals or organic light elements, which results in strong H_2 binding energy. However, this in turn brings about certain problems such as sluggish kinetics, irreversibility, the generation of byproduct, and the requirement of high energy to crack hydrogen out of metallic or organic compounds[123]. There have been numerous studies of methods to decrease the binding energy of covalently bonded H atoms[19,38,124] however, this problem remains unsolved.

This situation spurred us to revisit earlier reports of the hydrogen storage materials in an effort to find out some possible clues by which understand more deeply hydrogen storage behaviors in carbon nanopores in particular. As a result, we noted that the abnormal storage of H_2

molecules with liquid- or solid-like densities is possible in carbon nanopores with the average diameters of less than 1 nm[69,125-127], with little information about the scientific fundamentals. In fact, this type of abnormal phenomenon in carbon nanopores is not limited only to H_2 storage but extends to other cases such as high proton transport rates exceeding those of bulk water by an order of magnitude within CNT pores with a diameter of 0.8 nm[128], greatly enhanced charge storage in nanopores smaller than the size of a solvated electrolyte ion[129], and a variety of new ice phases formed by water molecules encapsulated in CNT nanopores[130]. These inspiring phenomena motivated us to attempt to understand the underlying scientific principles in depth. If the underlying mechanism could be unveiled, it may be possible to utilize it to develop new hydrogen storage materials and may provide clues by which to understand the above-mentioned and other similar abnormal phenomena in carbon nanopores with diameters in the sub-1nm range.

To elucidate the scientific fundamentals possibly involved in the liquid- or solid-like storage of hydrogen in carbon nanopores with sub-1 nm diameters, we attempt herein to find probable answers to two very critical questions : (a) What would induce the spontaneous inflow of H_2 molecules into sub-1 nm carbon nanopore, even though both are neutral?, (b) How can the H_2 molecules in the carbon nanopores be condensed having liquid- or solid-like densities? We noted studies of the structural phase transitions in materials under an external electric field or magnetic field[105-109] and surmised that this may be related to the phase transition of

H_2 molecules confined into the carbon nanopores, which deviates from the phase diagram of molecular hydrogen. Taken together, we formulated a hypothesis of hydrogen storage by intrinsic electromagnetic field (IEMF) interactions, with IEMF referring to an electromagnetic field formed by a material itself without an external energy source. To test our hypothesis, we herein verify the presence of an IEMF near a carbon nanopore with a diameter below 1 nm, the type of the interaction between the IEMF from the carbon nanopore and H_2 molecules, the effectiveness of the interaction, and the relationship between the IEMF and the H_2 storage behavior in the carbon nanopores in accordance with the critical questions mentioned above.

2.2. Experimental method

2.2.1. Computational studies

To describe the carbon nanopore, a cluster model of 4×4 bilayer graphene with an interlayer distance of 7.0 Å and the SWCNT with a diameter of 6.8 Å and length of 13.5 Å are chosen. Bilayer graphene consists of 96 carbon atoms and 36 hydrogen atoms with an unit cell size of 30 Å×30 Å×20 Å including a vacuum for all directions. The SWCNT consists of 120 carbon atoms and 20 hydrogen atoms with an unit cell size of 30 Å×30 Å×40 Å including a vacuum as well. The electron density calculations were conducted with DFT using the PBE exchange-correlation functional based on the projector augmented-wave (PAW) method implemented in the Vienna ab-initio simulation package (VASP). The plane-wave basis had an energy cutoff of 400 eV and the Brillouin zone was sampled using only the Γ point. Structure optimization was conducted until the variation in the energy was below 10^{-6} eV, and the electric potential energy including the London dispersion interaction was obtained by the DFT-D3 method.

Ab initio molecular dynamics (MD) simulations were performed to analyze the H_2 storage behavior of the SWCNTs and bilayer graphene at 300 K and 100 bar H_2. The temperature was maintained using a Nosé-Hoover thermostat with the time step fixed at 1 fs. The equilibration run lasted 2 ps (2000 time step) and at least a 30 ps (30000 time steps) production run was utilized to observe the H_2 storage behavior.

The electric field was calculated using the DFT charge density based on Gauss's law. The calculations were performed using COMSOL Multiphysics by setting the mesh size below 0.5 Å and the domain region to be a sphere that contains all data in the unit cell.

2.2.2. Materials

Natural graphite (Sigma-Aldrich), Potassium persulfate ($K_2S_2O_8$, 98%, Sigma-Aldrich), phosphorus pentoxide (P_4O_{10}, 98%, Sigma-Aldrich), ($KMnO_4$, 98%, Sigma-Aldrich), sulfuric acid (H_2SO_4, 98%, Daejung Chemicals & Metals), hydrogen peroxide (H_2O_2, 30%, Daejung Chemicals & Metals), and hydrochloric acid (HCl, 35–37%, Daejung

Chemicals & Metals). Single Walled Carbon Nanotubes (SWCNT, nanografi, 96%). Mesoporous carbon (CMK-3, ACS materials). All chemicals were used as-received.

2.2.3. Synthesis of freeze-dried graphene oxide

To increase the yield of graphene oxide, the graphite is oxidized with $K_2S_2O_8$ and P_4O_{10} before the main oxidation. 12 g $K_2S_2O_8$ and 12g P_4O_{10} were dissolved in 60 ml H_2SO_4 under 80 °C. 6 g of graphite was gradually added into the mixture. After 4 days, preoxidized graphite was obtained and it was poured into 2 L of deionized DI water. The washing and filtration were repeated until the filtrate water pH become neutral. Then it was dried in a vacuum oven at room temperature for 7 days. Graphene oxide is synthesized according to Hummers method. 2 g of preoxidzed graphite was dissolved into 92 ml H_2SO_4 while cooling to 5 °C and 12 g $KMnO_4$ was gradually added into the mixture. The reaction was conducted at 35 °C bath for 2 hours (step I oxidation). After 100 ml deionized water was added very carefully with temperature kept from 70 to 80 °C, further heat treatment at 95 °C for 2 hours were conducted (step II reaction). To stop the reaction 30 ml of H_2O_2 is injected and the mixture went through repeated HCl-washing and neutralization by using ultra-centrifugation at 13,000 rpm. The colloid was dried at room temperature for 1 day and it was freeze-dried for 48 hours using freeze-dryer (Bondiro, Ilshin Lab).

2.2.4. Porosity analysis and GHSC measurement

Because gas adsorption isotherm is essential to measure the specific surface area (SSA), CO2 isotherm at 300 K using BELSORP HP and N2 isotherm at 77 K using a Micromeritics ASAP2020. Non-local density functional theory (NL-DFT) was applied to N2 isotherm to determine pore size distribution. Prior to measurements, the all samples were degassed at 80 °C for 12 hours and the the Brunauer–Emmett–Teller (BET) method is applied to obtain the SSA. And 99.999% purity hydrogen high pressure gas adsorption analyzer (BELSORP HP) was used to measure GHSC at 300 K and 100 bar by a volumetric technique and the reliability/accuracy of the system were confirmed.

2.2.5. Characterization of structure of carbon nanomaterials

X-ray diffraction (XRD) was conducted using a D8 Advance (Bruker) diffractometer and Ni-filtered CuKα radiation (λ = 0.154184 nm) to confirm the interlayer distance of freeze-dried graphene oxide. Using atomic force microscopy (AFM, NX-10, Park Systems), non-contact mode AFM images and height profiles of the SWCNT were obtained to identify the its diameter. SWCNT was deposited on the Si/SiO2 substrate by spin-coating. Additionally, the diameter of SWCNT bundle is analyzed by employing transmission electron microscopy (TEM, Tecnai F20, FEI).

2.3. Result and discussion

2.3.1. Presence of IEMF near the carbon nanopore with a diameter of less than 1 nm

To identify whether the IEMF forms near the carbon nanopore, single-walled carbon nanotube (SWCNT) with a diameter of 6.8 Å and bilayer graphene with an interlayer distance of 7.0 Å were modelled to describe a cylindrical nanopore and a slit nanopore. IEMF is divided into intrinsic electric field (IEF) and intrinsic magnetic field, and firstly the IEF of nanopores are investigated. According to the calculation of the 3-D distribution of IEF near the nanopores, IEF in various directions was confirmed near both the SWCNT and the bilayer graphene (Figure 2.1A, 2.1B). It can be identified that this outward IEF forms very close to the nanopores and that the inward IEF forms primarily in other areas. It is surmised that the inward IEF is mainly due to the electrons and that the outward IEF is primarily due to the nuclei of the atoms. To investigate the distribution of the IEF strength, the IEF strength inside the tube (Figure 2.1C) is plotted as a function of the tube axis (z-direction) while that between the layers (Figure 2.1D) is plotted as a function of the y-direction including the center of the bilayer graphene. It was found that the IEF strength vanishes, becoming zero as the distance from the nanopores increases while IEF with an astonishingly large value (~ 10^9 V/m = ~1 V/nm) appears near the nanopores. These results suggest that contrary to our intuition, a piece of neutral material forms a significant electric field around it at the atomic level, similar to the action of a piece of charged material. On the other hand, these diamagnetic carbon nanomaterials[131-133] are not expected to form the intrinsic magnetic field as a consequence of an absence of current (no total electron spin) according to the Biot-Savart law ($B(r) = \frac{\mu_0}{4\pi}\int\frac{dI \times \hat{r}}{r^2}$). Therefore, it is concluded that a significant IEF-dominated IEMF (E-IEMF) arises near carbon nanopores due to the overlap of carbon walls without the application of an external energy source and any introduction of heteroatom. In this paper, the term, E-IEMF is used throughout the main text to emphasize that this hypothesis is also applicable to nanopores with magnetic properties.

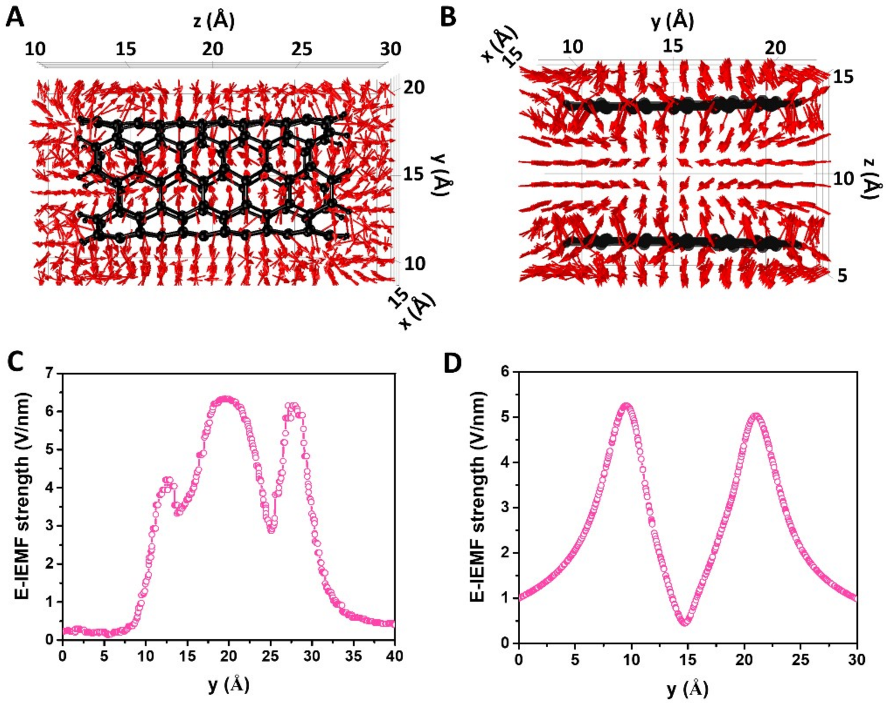

Figure 2.1. 3-D distribution of the E-IEMF direction of a cylindrical nanopore with a diameter of 6.8 Å (A) and a slit nanopore with an interlayer distance of 7.0 Å (B). 1-D line plot of the E-IEMF strength of the cylindrical nanopore (C) along the z-direction (x=15 Å, y=15 Å) and of the slit nanopore (D) along the y-direction (x=15 Å, z=10 Å).

2.3.2. The type of the interaction between the IEMF by the carbon nanopore and H_2 molecules and its effectiveness

It was previously identified that E-IEMF with various directions and non-uniform strength forms near the carbon nanopore. On that basis, a H_2 molecule near the carbon nanopore can be considered as a H_2 molecule under the E-IEMF, and this can be simplified to an electric dipole under a non-uniform electric field as shown in Figure 2.2. because a neutral H_2 molecule is electrically polarizable[134-136]. Consequently, it can be assumed that the H_2 molecule undergoes torque due to its alignment in the E-IEMF direction and is attracted to the strongest spot by the gradient of the E-IEMF along the inward E-IEMF direction. Therefore, H_2 molecules must experience attraction near the carbon nanopores, which is the principle of H_2 storage in sub-1nm carbon nanopores.

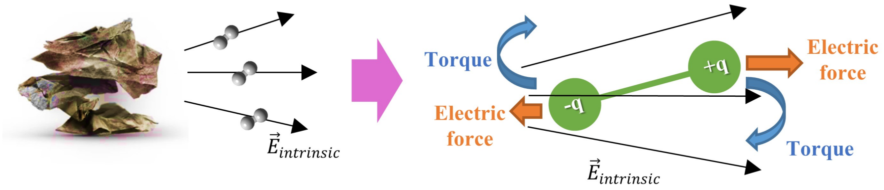

Figure 2.2. Simplified model of hydrogen storage by E-IEMF to electric dipole in non-uniform electric field. This shows the type of the IEMF interaction experienced by H_2 molecule.

This raises the question of whether the interaction is sufficient to induce H_2 polarization and override the thermal energy of the H_2 molecules. To measure the H_2 polarization, the induced maximum electric dipole moment of a H_2 molecule under the E-IEMF is calculated by referring to Figure 2.1C and 2.1D. The calculation reveals the average electric dipole moment of 0.20 Debye within the cylindrical nanopore and of 0.15 Debye within the slit nanopore, in reference to the electrical polarizability of the H_2 molecule[134-137]. Given the fact that the electric dipole moment of carbon monoxide, a polar molecule, is 0.12 Debye[138], it is concluded that the IEMF interaction effectively modulates the H_2 charge distribution. Next, the electric potential energy, the magnetic potential energy [139], and the thermal energy $(=\frac{5}{2}kT)$ of a H_2 molecule at 77 K and 300 K are compared to confirm the dominance of the IEMF interaction over the thermal energy (Table 1). The electric potential energy of the H_2 molecule is -207.2 meV within the cylindrical nanopore and -93.6 meV within the slit nanopore. No IMF results in magnetic potential energy of

0.0. meV, and the thermal energy of the H_2 molecule is +16.6 meV (77 K) and +64.7 meV (300 K). The overwhelming numerical value of the sum of the electric/magnetic potential energy signifies that the IEMF interaction effectively overrides the kinetic energy of the H_2 molecule.

Table 2.1. Comparison of the electric/magnetic potential energy of a H_2 molecule under the IEMF by the cylindrical/slit nanopore and the thermal energy of a H_2 molecule at 77 K and 300 K.

	Cylindrical nanopore	Slit nanopore
Electric potential energy of H_2 molecule	−207.2	−93.6
Magnetic potential energy of H_2 molecule	0.0	0.0
Thermal energy of H_2 molecule at 77 K (meV)	+16.6	
Thermal energy of H_2 molecule at 300 K (meV)	+64.7	

2.3.3. Relationship between the IEMF and H_2 storage behavior in the carbon nanopores

Above-mentioned results verify that the effective E-IEMF formed by the carbon nanopore attracts H_2 molecules inside the carbon nanopore and that the interaction between the IEMF and the H_2 molecule can effectively confine H_2 molecule in the carbon nanopore. As shown in Figure 2.1A and Figure 2.1B, the inward E-IEMF is identified at the edge of both nanopores, and this is assumed to be a starting point for the influx of H_2 molecules into the nanopore because they are attracted along the E-IEMF direction. This raises the question of how the pore geometry affects both the IEMF within the carbon nanopore and H_2 storage behavior although it just seems that the carbon nanopores are built by rolling up a piece of graphene or pile up two sheets of graphene. We surmise that each nanopore with a different geometry builds a different form of the IEMF, which leads to the difference of H_2 behavior within the carbon nanopore. To test this, the 3-D directional distribution of the E-IEMF inside the cylindrical nanopore and the interlayer space of the slit nanopore are investigated (Figure 2.3A, 2.3C). However, disordered E-IEMF is identified inside the former, while E-IEMF that converges to the center of the system in a consistent direction is found inside the latter. This means that the H_2 molecules introduced into the cylinder-shaped nanopore are subjected to various directional forces, while they experience a constant directional force within the slit-shaped nanopore.

To consider the effect of the E-IEMF strength distribution on the H_2 storage behavior, the 2-D distribution of the E-IEMF strength by the cylindrical nanopore with respect to the yz plane (x=15 Å) and that by the slit nanopore with respect to the xy plane (z=10 Å) are obtained (Figure 2.3B, 2.3D). The strongest E-IEMF in the center and weaker E-IEMF near the edges are spotted inside the cylindrical nanopore, while the strongest E-IEMF at the edges and weaker E-IEMF towards the center are identified in the slit nanopore. In conjunction with the distribution of the E-IEMF direction, it is presumed that the space with stronger electric force than the surrounding area that pushes from both sides to capture H_2 molecules is narrow in the cylindrical nanopore such that not many H_2 molecules are captured inside the cylinder nanopore, whereas it is so wide in the slit nanopore that many H_2 molecules are expected to fill the interlayer space. To compare the IEMF inside and outside the carbon nanopore, the E-IEMF of upper slit nanopore is investigated. On investigation of E-IEMF direction of upper slit nanopore, outward E-IEMF above the upper slit nanopore is found and inward E-IEMF forms elsewhere as presented in Figure 2E. Similar to the results inside the slit nanopore, very large E-IEMF strength (~1 V/nm) of upper slit nanopore is identified, however, the steadily stronger E-IEMF strength toward the center forms. Therefore, the E-IEMF in the form of well forms only inside nanopore by overlapping the carbon walls and it is thought that the resultant E-IEMF inside carbon nanopore can be strongly connected with the abnormal hydrogen storage phenomenon.

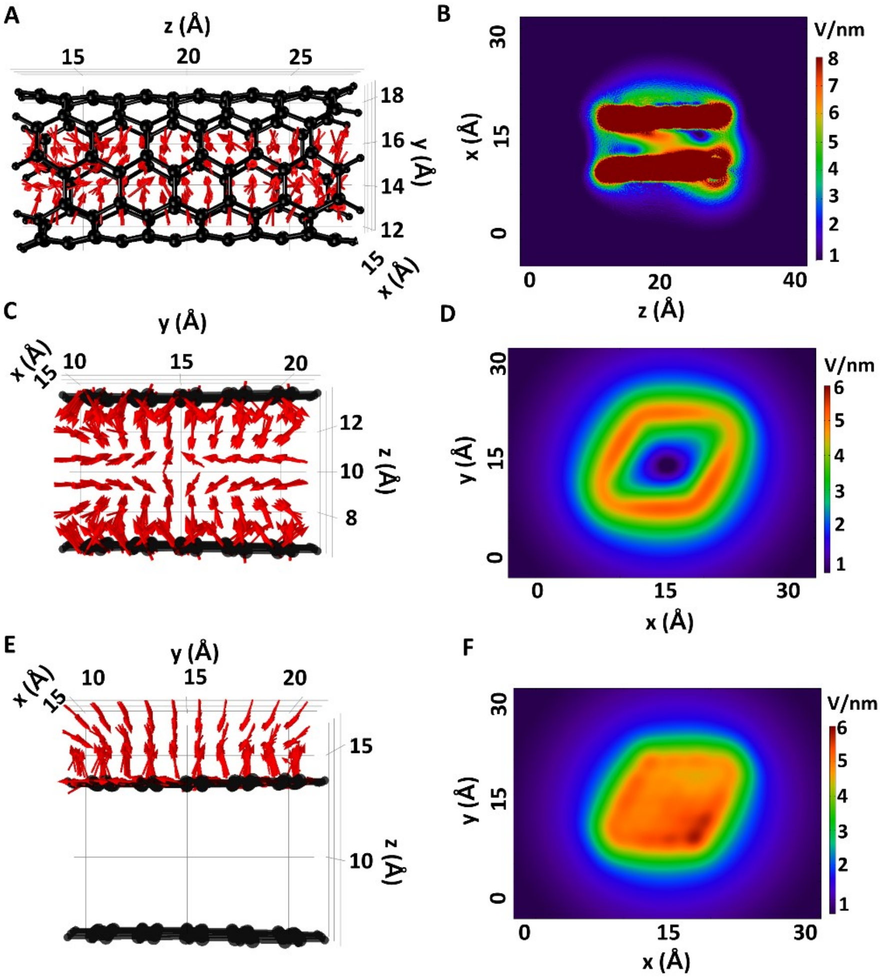

Figure 2.3. 3-D distribution of the E-IEMF direction (A) and 2-D distribution of the E-IEMF strength on the zy plane (x=15 Å) (B) inside the cylindrical nanopore. 3-D distribution of the E-IEMF direction (C) and 2-D distribution of the E-IEMF strength on the xy plane (z=10 Å) (D) in the interlayer space of the slit nanopore. (E) 3-D distribution of E-IEMF direction of upper slit nanopore. (F) 2-D distribution of E-IEMF strength of upper slit nanopore (z=16.5 Å)

To assure this, ab initio MD simulations of H_2 storage in an individual SWCNT and bilayer graphene were conducted. SWCNT with a diameter of 6.8 Å and length of 13.5 Å, and a cluster model of 4×4 bilayer graphene with an interlayer distance of 7.0 Å were used for the MD simulations at 300 K and under pressure of 100 bar H_2. The H_2 storage behavior within each system was monitored over time. For the SWCNT, 5 ps after the start of the MD simulation, the first H_2 molecule was captured inside the SWCNT. Over time, more H_2 molecules entered the SWCNT, however, more than three H_2 molecules were not be captured inside the SWCNT (Figure 2.4C). In contrast, it was observed that many more H_2 molecules could be captured in the bilayer graphene. As shown in Figure 2.4D, up to ~30 ps from the beginning, only two or three H_2 molecules were captured. However, over time, more H_2 molecules started to be captured, and after ~ 65 ps, 14 H_2 molecules were captured. It was observed that the H_2 molecules captured in bilayer graphene maintain a constant position and hardly move in place, confirming that they can be captured in the form of a two-dimensional solid-like phase. The GHSC of the SWCNT is 0.3 wt% and the H_2 density within the cylindrical nanopore of the SWCNT is 12 g/L, which exceeds the H_2 bulk density (8 g/L) under the same condition. The GHSC of the bilayer graphene is 2.3 wt%, which is 35% of the ultimate Department of Energy (D.O.E.) target for hydrogen storage and H_2 density within the slit nanopore of the bilayer graphene is 98 g/L, which exceeds solid H_2 density (87 g/L)[140]. This result is consistent with earlier experimental research that found that the density of H_2 molecules confined in a pore in size of 9 Å is roughly 60 g/L (80 g/L) at 300 K and 100 bar (200 bar) [69].

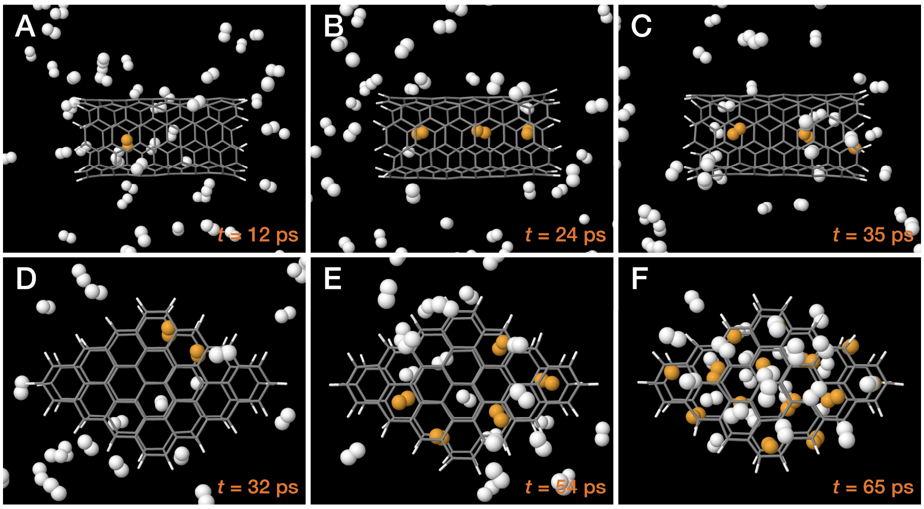

Figure 2.4. Snapshots of the MD simulation of H_2 storage into the SWCNT (A-C) with a diameter of 6.8 Å and length of 13.5 Å and bilayer graphene (D-F) with an interlayer distance of 7.0 Å. Gray and white sticks correspondingly represent the carbon atoms of the SWCNT/graphene and hydrogen atoms at the edges. White balls represent free H_2 molecules and orange balls represent captured H_2 molecules.

In addition, to augment our earlier conjecture and the simulation result experimentally, HDI (H_2 densification index) of the SWCNT powder with a diameter of less than 1 nm, freeze-dried graphene oxide with an interlayer distance of sub-1 nm and mesoporous carbon were obtained (see detailed description in Figure 2.5.).

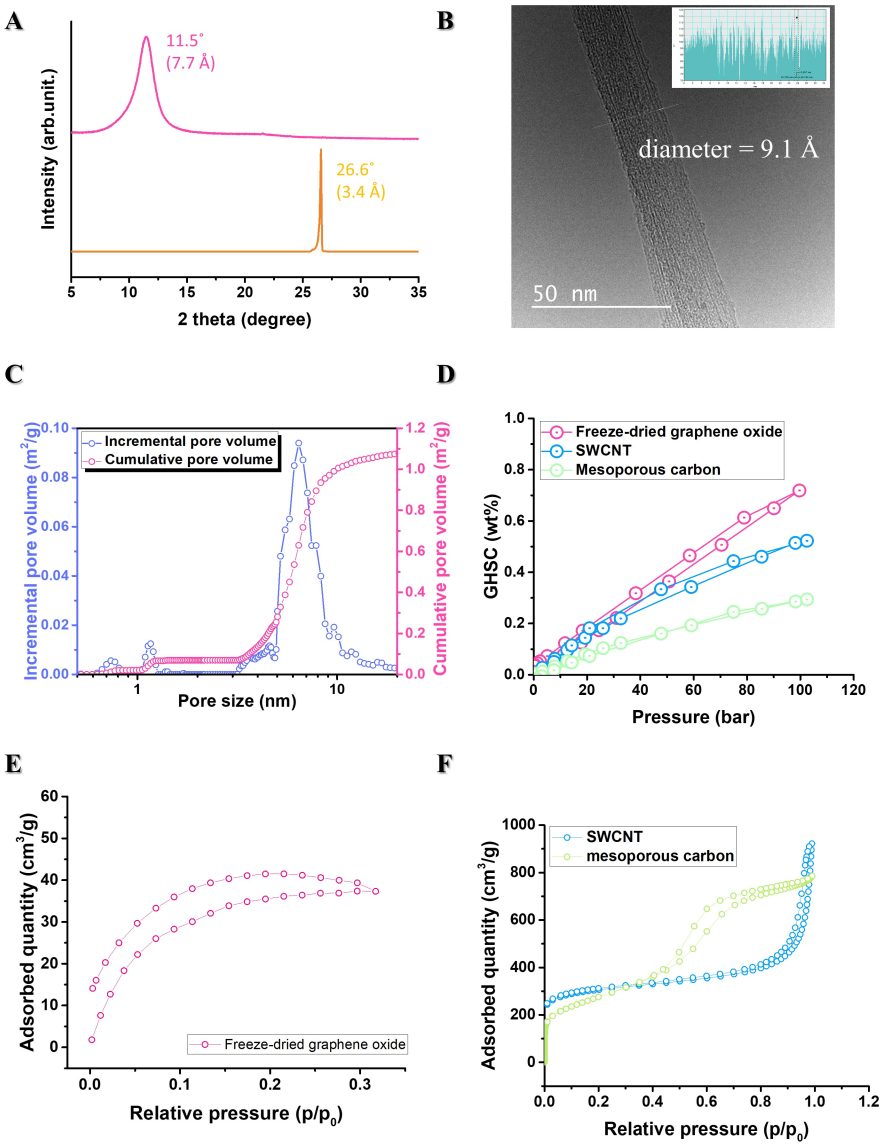

Figure 2.5. (A) XRD pattern of freeze-dried graphene oxide (red line) and natural graphite (orange line). (B) TEM image (C) of SWCNT bundle. (C) Pore size distribution of mesoporous carbon. The its main pore size is 6.4 nm. (D) GHSCs of freeze-dried graphene oxide with an interlayer distance of sub-1 nm, SWCNT powder with a diameter of less than 1 nm, and mesoporous carbon. All

are measured at 300 K and 100 bar. (E) CO2 isotherm at 300 K of freeze-dried graphene oxide to calculate SSA and its BET analysis. (F) N2 isotherms at 77 K of SWCNT and mesoporous carbon to calculate SSAs and their BET analysis.

Herein, a new term, HDI is suggested to normalize the effect of the specific surface area (SSA) of each sample on the GHSC and it is calculated by dividing GHSC × 10^4 into SSA. Upon a comparison with HDI, it is confirmed that the H_2 storage performance in freeze-dried graphene oxide is clearly superior (Figure 2.6). In consequence, it can be concluded that different geometries of the carbon nanopores form different IEMF and different H_2 storage behavior.

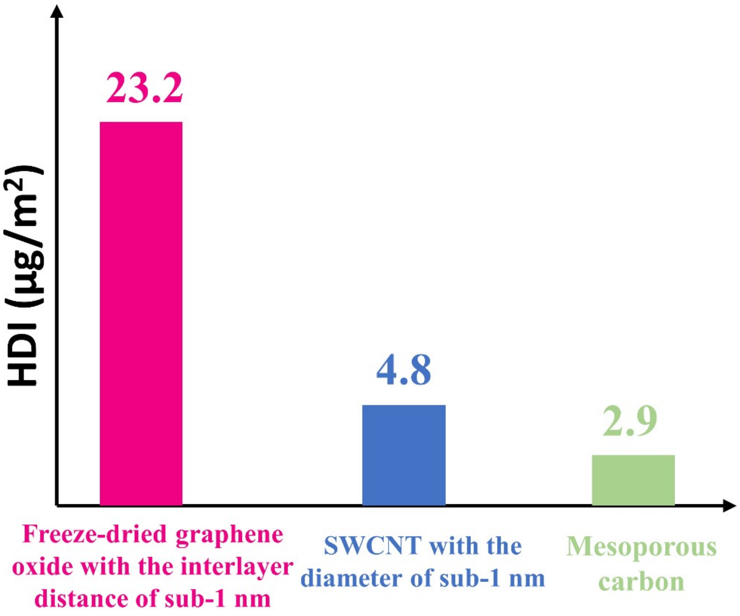

Figure 2.6. Comparison of the HDI of nanomaterials mainly containing slit nanopore, cylindrical nanopore, and mesopore. Note the superior H_2 storage performance of the materials with slit nanopore.

In the field of hydrogen storage research, the H_2 binding energy has been used to indicate a strong degree of H_2-material interaction and it is found at the lowest energy site to bind one H_2 molecule[53,68,141-144]. However, in this paper, it is demonstrated that the IEMF governs the H_2 storage behavior of carbon nanopores. Hence, it is thought that it may be more suitable to describe H_2-material interaction and to evaluate the GHSC from the perspective of the IEMF interaction rather than the H_2 binding energy, the previous governing parameter. Moreover, our work suggests that it may be possible to reach the D.O.E. target of hydrogen storage with modulation of the IEMF (e.g., control of the atomic composition) or via the irradiation of an external EMF. Furthermore, this work can be extended to other studies on the subject of abnormal phenomena in nanopores, which are reported superficially. That is, these results not only provide a clue for a potential breakthrough in the research on hydrogen storage materials but also bring new insight to other research on host-guest interactions.

2.4. Conclusions

We discussed the abnormal phenomenon in sub-1 nm carbon nanopores in case of hydrogen storage and revealed that the significant IEMF forms near sub-1nm carbon nanopores despite the fact that the carbon nanopores are neutral in charge. Moreover, the interaction between the IEMF and H_2 molecule is sufficient to modulate the charge distribution of H_2 molecules and override thermal energy of molecular hydrogen. Lastly, the relationship between the IEMF and H_2 storage behavior is investigated by conducting ab initio calculations and supplementary experiments, and it is shown that the IEMF governs the H_2 storage in the carbon nanopore and the morphology-induced IEMF inside the slit nanopore is closely connected to the abnormal H_2 storage behavior in nanopore. It is demonstrated that the H_2 density levels within cylindrical nanopore and slit nanopore are correspondingly 12 g/L and 98 g/L, clearly exceeding that (8 g/L) of freestanding H_2 molecules at 300 K and 100 bar, with the latter even exceeding that (80 g/L) of solid hydrogen. We unveil the H_2 storage mechanism with sub-1 nm diameters and offer a new perspective on hydrogen storage research directions. Furthermore, this work is not limited to research on hydrogen storage materials but can be extended to research on host-guest interactions or van der Waals interactions.

Chapter 3. Validation of effective IEMF modulation with variations in pore size and atomic composition.

3.1. Introduction

There is a bottleneck in the field of hydrogen storage to commercialize hydrogen energy[145,146]. Hydrogen storage materials have been studied to replace compressed hydrogen tanks currently in commercial use[1]. To date, researchers have conducted studies based on either the physisorption of H_2 molecules or the chemisorption of the H element. Physisorption has the merit of fast kinetics and good reversibility; however, the gravimetric H_2 storage capacity (GHSC) is too low due to it weak interaction. Thus, porous materials such as Metal-Organic Framework (MOF)[66], Covalent-Organic Framework (COF)[5,117], porous carbon[6] etc. have been developed to increase the specific surface area (SSA) or nanopores although consequently facing the limitations of technology to increase them. On the other hand, hydride-containing materials (e.g., metal hydrides[22], complex hydrides[14], chemical hydrides[19], organic molecules[32], etc) based on chemisorption are expected to exhibit a high GHSC however, have disadvantages of requiring high temperatures to overcome thermodynamic energy barriers, sluggish kinetics, and poor reversibility[123]. To solve these problems, efforts to lower the H_2 binding energy have been carried out, but a satisfactory result has not yet been achieved[3].

At this time, it is worth noticing the extraordinary phenomenon of dense liquid-like or solid-like H_2 storage in carbon nanopores[69,125-127,147], and previous researchers have superficially attributed this phenomenon to the potential overlap between the carbon walls[1,69,148,149] and have suggested no new research directions. Our group recently verified that the resultant intrinsic electromagnetic field (IEMF) by the overlap of IEMF of carbon nanopore walls is key to the extraordinary phenomenon and morphology-driven IEMF results in the different hydrogen storage behavior. Thus, from the perspective of practicality, the next question is how the IEMF is controlled and whether the IEMF modulation is correlated to the hydrogen storage performance. To date, many efforts to control the adsorption properties of carbon nanomaterial have been done and among them, control of the pore size[8,71,150-152] and introduction of heteroatoms into the carbon nanomaterial[43,153,154] are typical. We surmised that the IEMF could be modulated by tuning the pore diameter and atomic composition of the carbon nanopores.

Herein, this paper includes how to modulate IEMF effectively and the validity of the hydrogen storage by IEMF interaction.

3.2. Experimental method

3.2.1. Computational studies

DFT structural optimization and electron density calculation is performed using Vienna ab-initio simulation package (VASP). The plane-wave basis has an energy cutoff of 400 eV and the Brillouin zone is sampled using Γ-point only. Generalized-gradient approximation (GGA) of the Perdw-Burke-Ernzerhof (PBE) functional is used and van der Waals interaction correction is included using Grimme's DFT-D3 method. To describe the carbon nanopores with different pore diameters, the cluster models of 4×4 bilayer graphene with the interlayer distance of 6, 7 , 8, 9, and 10 Å are built. The Bilayer graphene consists of 96 carbon atoms and 36 hydrogen atoms with an unit cell size of 30 Å×30 Å×20 Å including a vacuum for all directions. To simulate N-doped carbon nanopore system, a cluster model of 4×4 bilayer graphene with an interlayer distance of 10 Å is chosen. Bilayer graphene without N doping consists of 96 carbon atoms and 36 hydrogen atoms and the unit cell size is 30Å×30Å×20Å including vacuum for all directions. One or two Pyrrolic N are introduced to at the edges of each graphene layer then total number of N atoms are two or four. Structural optimization is performed until the all the forces are less than 0.02 eV/Å and electron density is calculated under the self-consistent loop criterion of 10^{-6} eV. The electric field was calculated using the DFT charge density based on Gauss's law with COMSOL Multiphysics.

3.3. Result and discussion

3.3.1. Characteristics of the IEMF inside/outside the carbon nanopores based on the pore diameter and the effectiveness of the modulation

To describe carbon nanopores with different pore diameters, bilayer graphene with various interlayer distances from 6 to 10 Å was modelled, and the IEMF is considered as the combination of the intrinsic electric field and intrinsic magnetic field. According to the Biot-Savart law ($\vec{B}(r) = \frac{\mu_0}{4\pi}\int \frac{dl \times \hat{r}}{r^2}$), a diamagnetic carbon nanomaterial forms a negligible intrinsic magnetic field because the net electronic spin becomes zero, and indeed, carbon nanomaterials are known as diamagnetic material[131-133]. Therefore, it can be assumed that the intrinsic electric field-dominated IEMF (E-IEMF) forms in the bilayer graphene system. To assure this assumption, the 3-D distribution of the E-IEMF direction and 2-D distribution of the E-IEMF strength between the graphene layers were investigated as shown in Figure 3.1. It was found that an inward directional distribution of the E-IEMF between the layers is established and that its outward directional distribution near the nuclei is built irrespective of the interlayer distance (Figure 3.1A). It was assumed that the inward directional E-IEMF is mainly due to the electrons and that the outward thing is primarily due to the nuclei of the atoms according to

Gauss's law ($\nabla\cdot\vec{E} = \frac{Q}{\varepsilon_0}$). Next, it was found that contrary to our intuition, the E-IEMF with a surprisingly large strength (~ 10^9 V/m=~ 1 V/nm) forms between the graphene layers and that the overall E-IEMF strength increases as the interlayer distance of the bilayer graphene decreases, showing a stronger and then weaker tendency toward the center like a well (Figure 3.1B). Considering the distribution of both the IEMF direction and strength, it was assumed that a neutral hydrogen molecule under the E-IEMF between the graphene layers becomes an electric dipole, dragged inside the interlayer space, and is finally confined inside the interlayer space because the strongest electric force is at the edge of the bilayer graphene. This concept is suggested to be the working principle of the abnormal hydrogen storage in carbon nanopores, which was previously reported by our group.

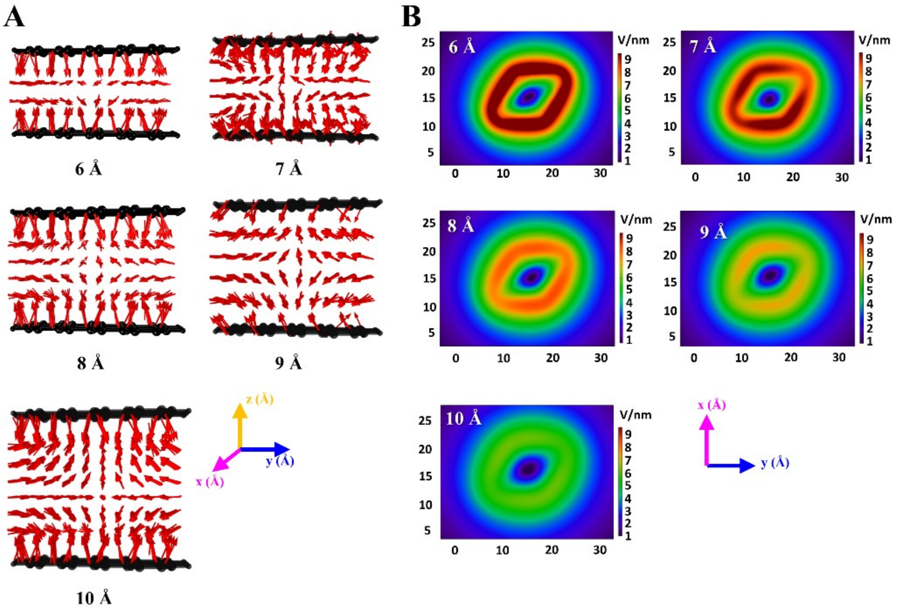

Figure 3.1. (A) 3-D distribution of the E-IEMF direction of the interlayer of the bilayer graphene with different interlayer distances from 6 to 10 Å. (B) 2-D distribution (xy plane, z=10 Å) of the E-IEMF strength of the interlayer of the bilayer graphene with different interlayer distances from 6 to 10 Å.

To compare the difference between the E-IEMF inside and outside the nanopores, the 3-D distribution of the E-IEMF direction and 2-D distribution of the E-IEMF strength of the upper bilayer graphene were analyzed as shown in Figure 3.2. The outward E-IEMF above the upper plane of bilayer graphene is found, and the inward E-IEMF forms from the far place, all of which are irrelevant to the interlayer distance of bilayer graphene (Figure 3.2A). Similar to the results of the interlayer of the bilayer graphene, a very large E-IEMF strength (~ 10^9 V/m=~ 1 V/nm) of the upper bilayer graphene is identified as shown in Figure 3.2B. In contrast to the results of the interlayer of the bilayer graphene, it is identified that the steadily stronger E-IEMF is formed toward the center. Combining the above-mentioned results, it is assumed that a neutral hydrogen molecule under the E-IEMF of the upper bilayer graphene becomes an electric dipole and is dragged onto the upper surface of the bilayer graphene. However, the steady increase of the E-IEMF toward the center with no electric force pushing from both sides cannot confine the hydrogen molecule, which is different from the case of the interlayer space. Summing up the above results, it can be concluded that the overlap of the IEMF of each graphene layer creates a special space where the

IEMF fits to confine guest molecules spreads out and the resultant IEMF strength can be modulated effectively by controlling the degree of overlap.

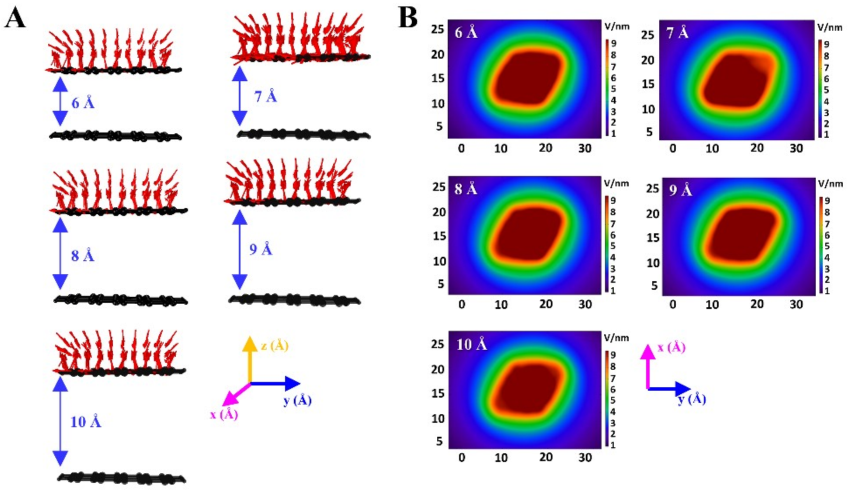

Figure 3.2. (A) 3-D distribution of the E-IEMF direction of the upper bilayer graphene with different interlayer distance from 6 to 10 Å. (B) 2-D distribution (xy plane, z=18 Å) of the E-IEMF strength of the upper bilayer graphene with different interlayer distances from 6 to 10 Å.

3.3.2. The variation in the IEMF inside/outside the carbon nanopore based on the heteroatom contents and its effectiveness

To investigate the effect of introducing heteroatoms into the carbon nanopores on the IEMF modulation, N-doped bilayer graphene with different N content was modelled, and its interlayer distance was fixed at 10 Å to minimize the effect of overlapping the IEMF of the two graphene layers. Referring to the previous computational studies[155,156], pyrrolic nitrogen, which is the most advantageous for hydrogen storage was introduced to the bilayer graphene and three models with a N content of 0.0, 2.2, and 4.4 at% were built. The IEMF is divided into an intrinsic electric field and intrinsic magnetic field, and the latter of the bilayer graphene with a small N content is not expected to form as reported earlier because it shows a non-ferromagnetic property [157,158]. Thus, it is assumed that the E-IEMF forms near N-doped bilayer graphene, and the 3-D distribution of its direction and 2-D distribution of its strength were obtained. As the N content increases, a slight change in the distribution of the IEMF direction is identified. Additionally, it is found that the up and down symmetry is broken in the E-IEMF direction as shown in Figure 3.3A. However, the general trend that the outward E-IEMF forms near the nuclei of the atoms and the inward E-IEMF forms in the remaining spaces is maintained, thereby avoiding the disruption of the hydrogen influx. Next, it is found that the introduction of nitrogen into the bilayer graphene does not change the trend of an increasing and then weakening E-IEMF strength like a well as shown in Figure 3.3B. It is noteworthy that the overall E-IEMF strength increases as the N content increases and the particularly enhanced E-IEMF is formed locally on the opposite side of the place where the nitrogen is introduced. The positions of the introduced nitrogen atoms are presented in Table S1. Therefore, the heteroatom-induced IEMF modulation is effective, and consequently the control of the hydrogen storage performance by controlling the atomic composition is believed to be possible because the E-IEMF inside the nanopores governs the H_2 storage behavior as mentioned previously.

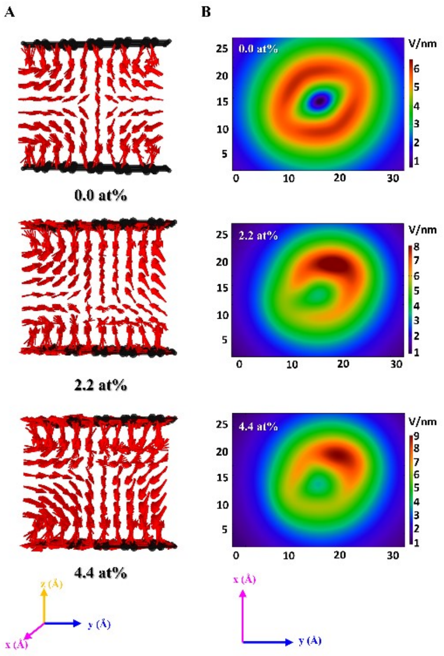

Figure 3.3. (A) 3-D distribution of the E-IEMF distribution of the interlayer of the bilayer graphene with an increment of the N content. (B) 2-D distribution of the E-IEMF strength of the interlayer of the bilayer graphene with different N contents. Note the overall increase of the E-IEMF strength with the N content.

To compare the difference between the IEMF inside and outside the nanopore, the 3-D distribution of the E-IEMF direction and the 2-D distribution of the E-IEMF strength of the upper N-doped bilayer graphene were investigated. The outward E-IEMF above the upper plane of the N-doped bilayer graphene is found, and the inward E-IEMF is formed from the far place, all of which are irrespective of the N content

(Figure 3.4A). While the distribution of the E-IEMF strength in the form of a well is identified in the interlayer of the N-doped bilayer graphene, the steadily stronger E-IEMF strength is found in the upper N-doped bilayer graphene. Put together, it is concluded that the overlap of the E-IEMF of each N-doped graphene layer creates the critical space where the IEMF is favorable for confining hydrogen molecules and that the resultant IEMF strength can be practically modulated by introducing heteroatoms. On the other hand, it is identified that the realm of the strongest E-IEMF strength of the N-doped bilayer graphene with a N content of 4.4 at% suddenly shrinks while its maximum value is almost maintained as shown in Figure 3.4B.

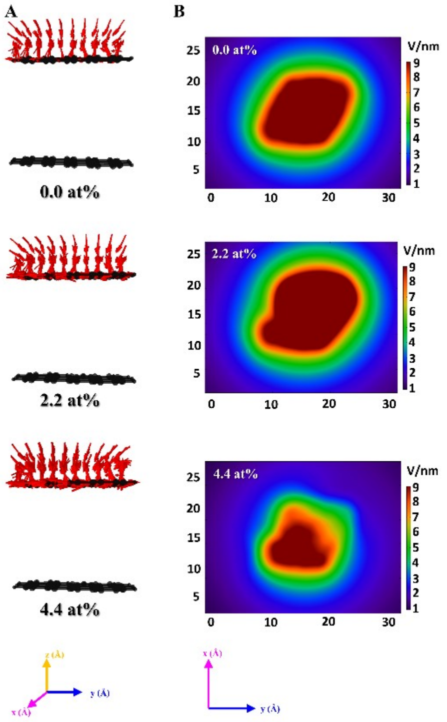

Figure 3.4. (A) 3-D distribution of the E-IEMF distribution of the upper bilayer graphene with an increment of N content. (B) 2-D

distribution of the E-IEMF strength of the upper bilayer graphene with different N contents.

3.4. Conclusions

The research field of hydrogen storage requires innovative research and the eccentric hydrogen storage phenomenon in the carbon nanopore with the diameter of sub-1 nm is remarkable. Recently, it was discovered that this phenomenon is caused by IEMF interaction and we raised questions about how to modulate the IEMF. To solve the questions, the distribution of IEMF direction and IEMF strength of bilayer graphene with different interlayer distance and different N content is analyzed. For both cases, it is discovered that the specific distribution of IEMF only forms in the interlayer space, and this affects hydrogen storage behavior critically.

Chapter 4. Investigation of correlation between HDI and IEMF strength within the specific systems.

4.1. Introduction

It was verified that hydrogen storage is caused by IEMF interaction and the IEMF can be modulated by controlling pore size and atomic composition of carbon nanomaterial. Thus, I can raise the question of whether the IEMF modulation correlates hydrogen storage performance of carbon nanomaterial. Herein, it is verified that the IEMF is highly correlated to hydrogen storage performance.

4.2. Experimental method

4.2.1. Materials

α-D-Glucose (Aldrich), lithium nitrate (Aldrich), lithium chloride (Aldrich), potassium chloride (Aldrich), and hydrochloric acid (HCl; Daejung, Korea).

4.2.2. Synthesis of N-doped porous carbon

A carbohydrate (α-D-Glucose), reactive salt ($LiNO_3$), and eutectic mixture (LiCl/KCl = 45/55 by weight) were mixed in the weight ratio of reactants/solvent = 1:10 (solvent: LiCl/KCl). The reactants are a mixture of $LiNO_3$ and glucose in a 1:1 weight ratio. The powders were homogenized with a ball mill. The powder mixture was filled into a alumina crucible and then transferred to the tube furnace with a continuous nitrogen flow. After flushing with nitrogen for 100 min, the furnace was ramped at 5 ℃ min^{-1} to reaction temperature and kept this temperature for 5 h to allow complete conversion. The furnace was naturally cooled to ambient temperature, meanwhile, the nitrogen flow was maintained until the temperature reached below 40 ℃. The as-obtained products which contained carbon the different salts were crushed into powders. Then, the powders were dispersed in sufficient amount of water to dissolve the salts. In some cases, the carbon samples synthesized at high temperature was washed with a dilute HCl solution to remove insoluble residuals. The carbon was obtained from the dispersion through vacuum filtration. The samples were dried in a vacuum at 65 ℃ for over 24 h. The as-obtained samples are denoted as NDC_X (X: synthesis temperature) for N-doped mesoporous carbons.

4.2.3. Material characterization

For structural characterization, Powder X-ray diffraction (XRD) was conducted from 5° to 50° using a step size of 0.02° and a run time of 2 sec/step at operation conduction of 40 kV and 40 mA using a D8 Advance (Bruker) with Ni-filtered CuKα radiation (λ = 0.154184 nm). Raman spectroscopy (RAMAN; force K VIS-IUS, Nanophoton) was conducted using a 532-nm laser to analyze the surface chemical structure of the products. Scanning electron microscopy (SEM; S-4300, Hitachi) and transmission electron microscopy (TEM;JEOL Ltd 2100F) was used to identify the morphological structure. X-ray photo-emission spectroscopy (XPS;AXIS-His, KRATOS) were employed to analyze the surface chemical properties. Nitrogen adsorption isotherms at 77 K up to 1 bar were recorded using a Micromeritics ASAP2020 to calculate the SSA based on the Brunauer–Emmett–Teller (BET) method. GHSC of NDC samples were measured under high-pressure conditions (up to 100 bar) at 300 K using a magnetic suspension microbalance with a resolution of 30 μg (Rubotherm). Prior to H_2 measurement, vacuum treatment (~10^{-9} bar) at 373 K overnight were conducted and H_2 with high purity (99.9999%) was used.

4.3. Result and discussion

4.3.1. The correlation of the IEMF modulation with the hydrogen storage performance and the reliability of the governing parameters that describe the hydrogen storage phenomenon

Before investigating the correlation of the IEMF modulation inside the bilayer graphene with hydrogen storage performance, we designated a new term the E-IEMF well as a representative index to describe the hydrogen storage by the IEMF interaction because the confinement of hydrogen molecules is connected with the form of the well of E-IEMF, and the E-IEMF well is obtained by integrating the overlapped area of black and yellow (Figure 4.1A). It is found that the calculated E-IEMF well decreases as the interlayer distance of the bilayer graphene increases (Figure 4.1B). The HDI is calculated by referring to the reported results of the hydrogen storage performance of the bilayer graphene at 300 K and 100 bar [72,75], and the HDI is plotted as a function of the E-IEMF well concerning to the bilayer graphene with different interlayer distances as shown in Figure 4.1C. The plot shows that the HDI increases as the E-IEMF well increases and that the modulation of E-IEMF by controlling the pore diameter is effective to control hydrogen storage performance. Before investigating the validity of the E-IEMF well, the plot of the HDI as a function of the H_2 binding energy is shown in Figure 4.1D, and the validity of the H_2 binding energy, which is the previous governing parameter in the research field of hydrogen storage is verified. As a result of investigating the relationship between the E-IEMF and the H_2 binding energy as shown in Figure 4.1E, a high correlation between the two parameters are found, indicating that the E-IEMF well is a reliable parameter.

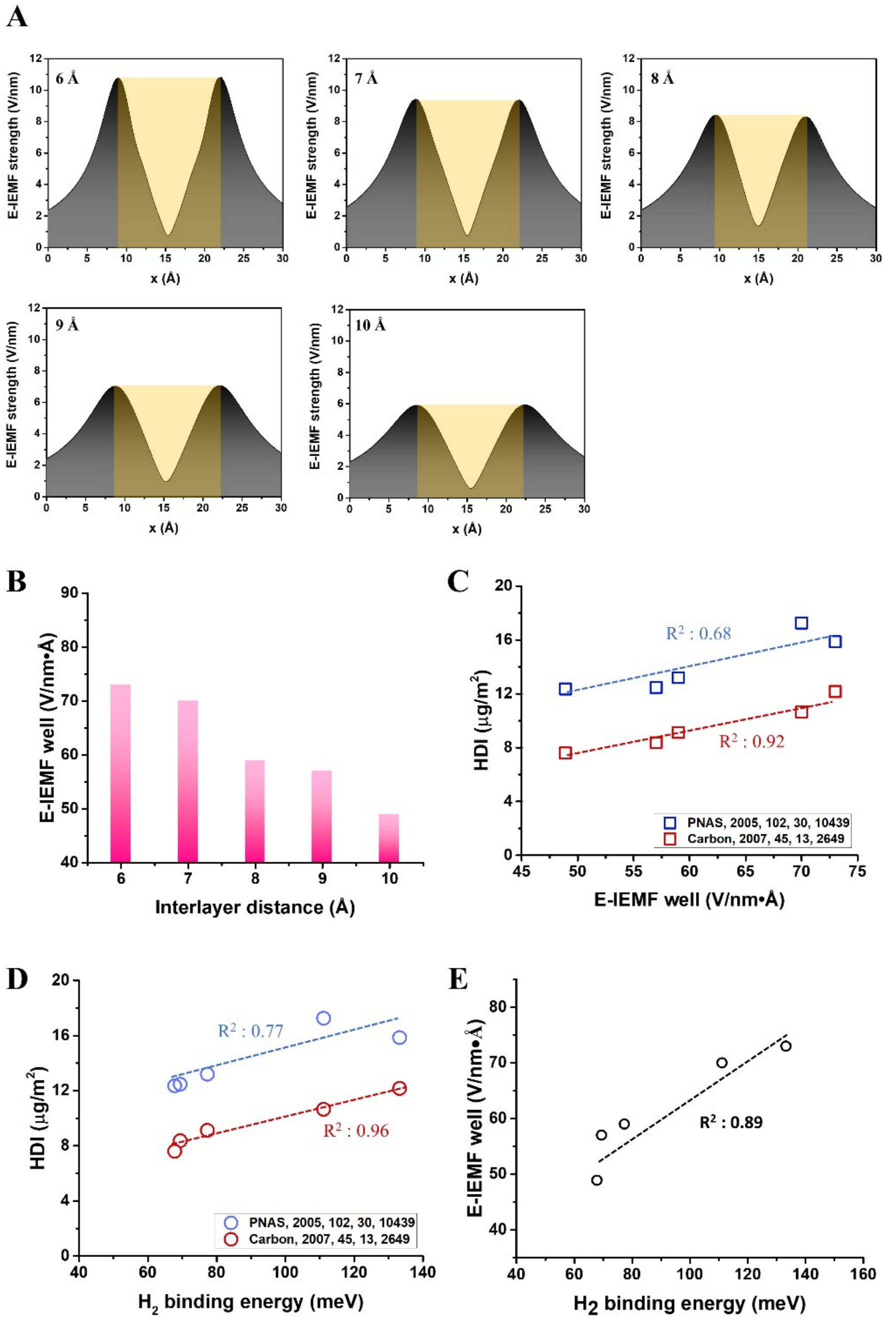

Figure 4.1. (A) 1-D line graph of the E-IEMF strength of the interlayer of the bilayer graphene with different interlayer distance along x-direction (y=15 Å and z= 10 Å). (B) Plot of the E-IEMF well of the interlayer of the bilayer graphene with its different interlayer

distances. (C) Relationship between the HDI and E-IEMF well. (D) Correlation of the HDI with the H_2 binding energy. (E) Correlation between the E-IEMF well and H_2 binding energy.

4.3.2. The connection between the IEMF modulation and hydrogen storage performance & the validity of the governing parameters that describe the hydrogen storage phenomenon

To verify the correlation of the IEMF modulation by the introduction of heteroatoms with the hydrogen storage performance, N-doped porous carbons were synthesized through the molten-salt method[159], and their surface characteristics, GHSC, SSA, and atomic composition were measured and presented in Figure 4.2.

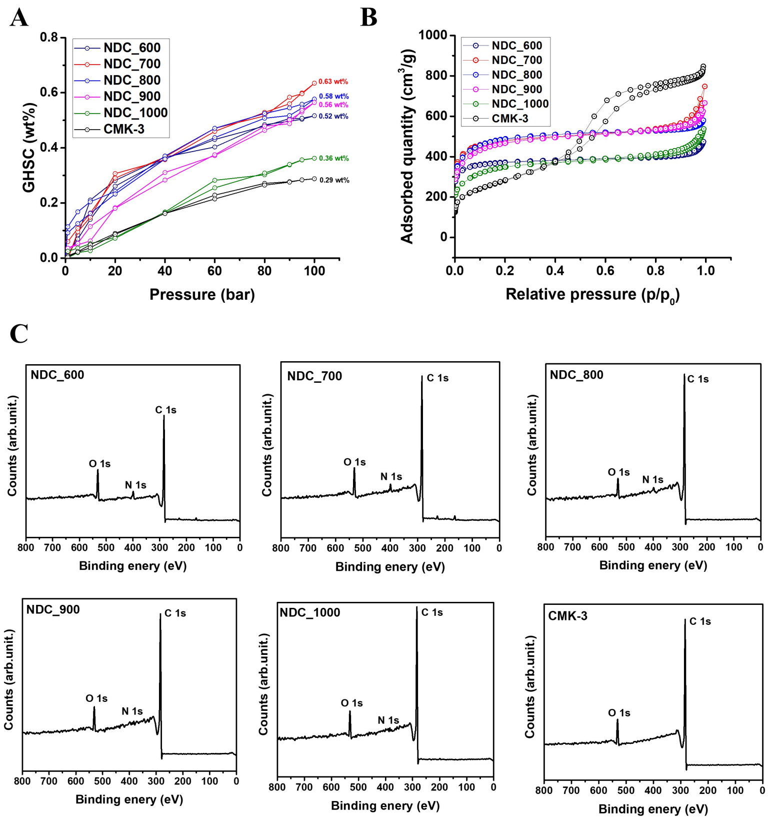

Figure 4.2. (A) GHSCs of N-doped porous carbons and CMK-3. (B) N2 isotherm at 77 K of all samples. (C) XPS wide scan spectra of N-doped carbons and CMK-3.

As mentioned earlier, the confinement of the hydrogen molecules is connected with the form of well of E-IEMF and thus, the E-IEMF well is thought of as an indicator of the hydrogen storage by the IEMF interaction. Before obtaining the estimates of the E-IEMF well corresponding porous carbon and N-doped porous carbons, the E-IEMF well of the N-doped bilayer graphene models was calculated from the 1-D line graph of the E-IEMF strength of the interlayer of N-doped bilayer graphene models along x-direction (y=15 Å and z= 10 Å) as shown in

Figure 4.3A. Then, the estimates of the E-IEMF well of porous carbon and N-doped porous carbons were obtained by interpolating the previously calculated E-IEMF well of the N-doped bilayer graphene models as shown Figure 4.3B. On that basis, as a result of plotting the HDI as a function of the E-IEMF well for the porous carbon and N-doped porous carbons, it is found that the HDI increases as the E-IEMF well increases (Figure 4.3C), and it is concluded that the introduction of heteroatoms into carbon nanomaterials is effective to enhance the hydrogen storage performance. To verify the validity of the H_2 binding energy which is the previous governing parameter in the research field of hydrogen storage, the H_2 binding energies in the N-doped bilayer graphene models with different N content were obtained as shown in Figure 4.3D, and it is found that the H_2 binding energy with the increase of the N content does not change remarkably while it shows an increase and then a decrease. The difference between the two correlations of the HDI with the H_2 binding energy and the E-IEMF well results from the fact that the former is determined by one-point, while the latter covers the space where the hydrogen molecules are captured, which shows the validity of the E-IEMF well again. Summarizing the obtained E-IEMF well in this paper, it is found that the decline of the E-IEMF as the interlayer distance increases recovers with the increase of the N content as shown in Figure 4.3E. This striking result suggests that pores larger than 1 nm in diameters can also have a significant role in hydrogen storage by introducing heteroatoms, which is in contrast to the previously known fact that only sub-1 nm nanopores can be effective in the hydrogen storage[151,160-162].

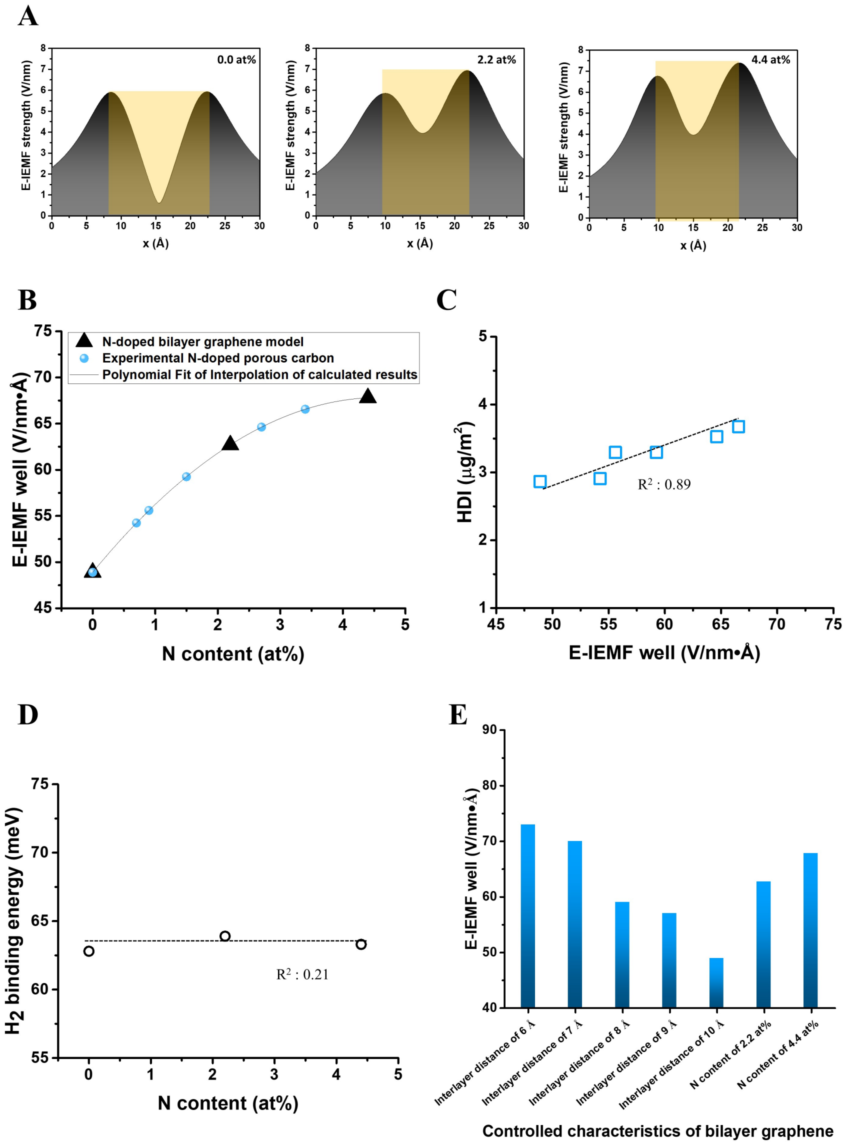

Figure 4.3. (A) 1-D line graph of the E-IEMF strength of the interlayer of the N-doped bilayer graphene along the x-direction (y=15 Å and z= 10 Å). Overlapped area of yellow and black is the area for the calculation of the E-IEMF well. (B) Trend of the E-IEMF well of

the interlayer of the theoretical N-doped bilayer graphene model and experimental porous carbon and N-doped porous carbons. The E-IEMF well of the latter is obtained by interpolating that of the former. (C) Plot of the HDI as a function of the E-IEMF well, showing a high correlation. (D) Relationship between the H_2 binding energy and the N content. Note their poor correlation. (E) All obtained E-IEMF well in this paper by controlling the interlayer distance or N content of the bilayer graphene.

4.4. Conclusions

The research field of hydrogen storage requires innovative research and the eccentric hydrogen storage phenomenon in the carbon nanopore with the diameter of sub-1 nm is remarkable. Recently, it was discovered that this phenomenon is caused by IEMF interaction and we raised questions about how to modulate the IEMF and whether its correlation to hydrogen storage performance exists. In this chapter, it is verified that IEMF modulation is highly correlated to hydrogen storage performance, showing the validity of IEMF interaction and the possibility of making a breakthrough in the development of hydrogen storage materials. Furthermore, since our research covers not only hydrogen storage materials but also host-guest interaction, it is expected to have a striking ripple effect on other research fields (e.g., supercapacitor, battery, catalyst).

Chapter 5. Preparation and characterization of carbon-based material with adjustment to the pore size and atomic composition

5.1. Introduction

Hydrogen energy is paid attention in that it has high gravimetric energy density, it is an abundant element in the universe, it is renewable energy, and it doesn't emit green-house gases, thereby being eco-friendly. To move toward hydrogen economy, the storage of hydrogen is important because large amounts of hydrogen should be transported to other places. To date, the technologies of compression and liquefaction are widely used and they are required to solve the technological obstacles such as safety issue in the former and boil-off issue in the latter. For this reason, adsorption-based solid hydrogen materials are attracting, and they mainly store hydrogen by chemical and physical adsorption. Materials to exploit chemical adsorption include metal hydride, complex hydride, ammonia borane, organic molecules, etc., are expected to store a large amounts of hydrogen; however, high thermal energy is required for adsorption/desorption, which means that they are inappropriate to be used at room temperature. Though hydrogen storage at room temperature is possible by using physical adsorption, its very weak interaction results in low gravimetric hydrogen storage capacity (GHSC). Fortunately, the eccentric phenomenon that hydrogen storage of liquid- or solid-like density levels is possible in the carbon nanopore with the dimeter below 1 nm has been reported. Patchkovskii et al. verified the high density of hydrogen molecules confined into bilayer graphene of 56 g/l at 300 K and 100 bar, showing that the interaction energy between the H_2 and bilayer graphene increases as its interlayer distance decreases [72] . Gallego et al. reported the solid-like density of hydrogen molecules captured into the carbon nanopore of roughly 80 g/l at 300 K and 200 bar by using inelastic neutron scattering, confirming the densification effect of carbon nanopore of sub- 1nm [69]. On the other hand, researchers have made efforts to functionalize carbon nanomaterials by introducing heteroatoms, thereby breaking the delocalized sp^2 system, creating its surface polarization and increasing the interaction energy between the H_2 and them. Herein, we successfully synthesize nitrogen plasma-treated N-doped microporous carbon that contains large pore volume below 1 nm and small amount of nitrogen and measure its hydrogen storage performance at room temperature.

5.2. Experimental method

5.2.1. Synthesis of N-doped microporous carbon (MC)

MC is purchased from Kansai Coke and Chemicals (Japan). The nitrogen plasma treatment was conducted with a radio frequency (RF) plasma system made by Femto Science (South Korea) equipped with high purity N_2 gas. The plasma was generated by RF of 90 W and 50 kHz. The MC in a vacuum reacted with nitrogen plasma for 3, 5, 7, and 9 min and the sample code was denoted as MC_NX (X : reaction time).

5.2.2. Material Characterization and hydrogen storage performance measurement

X-ray photo-emission spectroscopy (XPS; K-alpha+, Thermo Fisher Scientific, USA) were employed to analyze the surface chemical properties. Nitrogen adsorption isotherms at 77 K up to 1 bar were recorded using a Micromeritics ASAP2020 to calculate the SSA based on the Brunauer–Emmett–Teller (BET) method and the pore size distribution is obtained by Nonlocal density functional theory (NLDFT) method. Hydrogen storage performance of each sample of 300 mg or more was measured under high-pressure conditions (up to 100 bar) at 300 K using volumetric apparatus (Belsorp-HP, Japan). Prior to H_2 measurement, vacuum treatment ($\sim 10^{-9}$ bar) at 373 K overnight were conducted and H_2 with high purity (99.9999%) was used.

5.3. Result and discussion

5.3.1. Surface characteristics and atomic composition of N-doped MC

To investigate surface characteristics of MC and N-doped MCs, the calculation of SSA and the analysis of pore size distribution are essential. N_2 isotherm at 77 K of all samples are presented in Figure5.1A and different total adsorbed N_2 quantities signify that total pore volume is change as the nitrogen plasma treatment time. Moreover, as a result of calculation of SSA of each sample, it is found that the SSA of MC, MC_N3, MC_N5, MC_N7, and MC_N9 are 2040, 2186, 2448, 2250, and 2100 m^2/g, respectively. It is notable that the SSA increases and then decreases as the nitrogen plasma reaction time increases, showing the SSA of MC_N5 is the highest. To study the porosity of samples further, the pore size distribution of each sample is analyzed as presented in Figure 5.1B. The total pore volume (pore volume with a diameter of sub-1 nm) of MC, MC_N3, MC_N5, MC_N7, and MC_N9 are 0.94 (0.52), 1.00 (0.52), 1.09 (0.57), 1.02 (0.51), and 0.92 (0.50) cm^3/g and MC_5 show the outstanding porosity with the highest SSA, largest total volume, and largest pore volume with a diameter of sub-1 nm. The latter of MC_5 is roughly 10% larger than that of MC, which is expected to increase hydrogen storage performance. It is assumed that the plasma etching process induces such porosity and the excessive etching effect results in loss of pore [163].

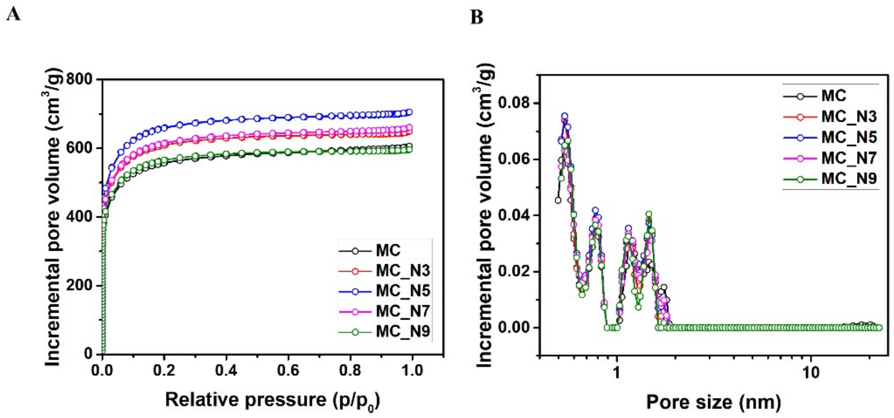

Figure 5.1. (A) N_2 isotherm of MC and N-doped MCs at 77 K. (B) Pore size distribution of each sample, obtained by NLDFT method.

Next, the atomic composition of MC and N-doped MCs are analyzed with XPS. The XPS wide scan of each sample is presented in Figure 5.2A and from this, the introduction of N into MC is confirmed while MC is made up of C, O atoms. It is found that the N content of MC_N3, MC_N5, MC_N7, and MC_N9 is 1.2, 1.3, 1.4, and 1.7 at% and the N content of N-doped porous carbon increases as the nitrogen plasma reaction time increases. On the other hand, the maintained O content of MC_N3, MC_N5, MC_N7, and MC_N9 is identified while their O contents increase after nitrogen plasma treatment. This is because a small amount of moisture remains during plasma treatment or the adsorbed oxygen gas onto N-doped polar surface is detected during XPS analysis [163]. To show the introduction of N clearly and confirm the possibility of effect of different nitrogen species on hydrogen storage performance [155,156], XPS N 1s core level spectrum of N-doped porous carbon is presented, finding that pyrrolic, pyridinic, amine, and graphitic N are distributed as shown in Figure 5.2B. It is confirmed that the ratio between nitrogen species is almost maintained irrespective of nitrogen plasma treatment time and thus, the effect of nitrogen species on hydrogen storage performance is assumed to be negligible in this research. To show the characteristics and composition of samples clearly, the above-mentioned results are summarized in Table 5.1.

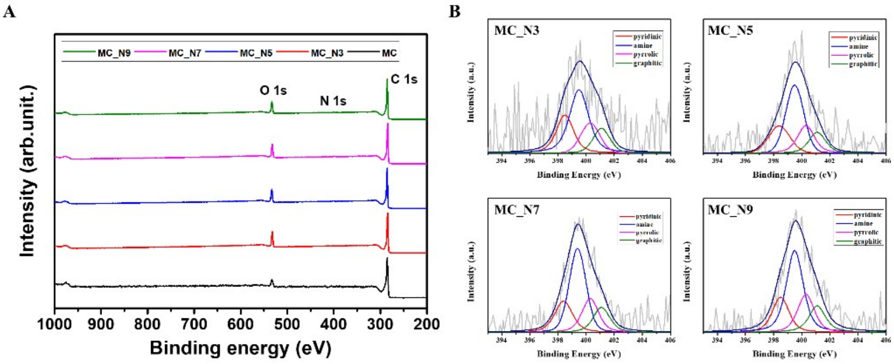

Figure 5.2. (A) The XPS full spectra of each sample. (B) XPS N 1s core level spectrum of N-doped porous carbon to show the introduction of N clearly.

Table 5.1. Surface characteristics and compositions of MC and N-doped MCs

Sample code	**MC**	**MC_ N3**	**MC_ N5**	**MC_ N7**	**MC_ N9**
Sub-1nm micropore volume (cm^3/g)	0.52	0.52	0.57	0.51	0.50
Total Pore volume (cm^3/g)	0.94	1.00	1.09	1.02	0.92
SSA (m^2/g)	2040	2186	2448	2250	2100
C content (at%)	92.6	85.5	85.3	85.4	85.9
N content (at%)	0.0	1.2	1.3	1.4	1.7
O content (at%)	7.4	13.3	13.4	13.3	12.4
Pyridinic	-	23.93	21.19	20.12	19.07
Amine	-	44.07	44.30	44.63	44.85
Pyrrolic	-	17.73	20.01	20.15	20.60
Graphitic	-	14.27	14.49	15.10	15.48

5.3.2. Hydrogen storage performance at room temperature

The H_2 storage performance at 300 K and 100 bar was measured and shown in Figure 5.3. The increase of GHSC of MC_N3, MC_N5, and MC_N7 are shown compared to that of MC and this findings is attributed to the increase of sub-1nm micropore and the introduction of N defect. Specifically, the MC_N5 exhibits 15% higher performance than raw material, MC, and it is notable that it is the higher performance than that of MC_N7 and MC_N9 with higher N content. The degradation of MC_N7 and MC_N9 by excessive plasma treatment is attributed to the lower performance and consequently, it is concluded that the emergence of sub-1nm pore is more significantly effective on increase hydrogen storage performance.

In fact, the measured GHSC by volumetric apparatus considers the quantity of captured hydrogen molecules, which is called excess GHSC [164]. To evaluate the practicality of samples as a hydrogen storage material, total GHSC is calculated by considering the total pore volume to be the stored volume of free hydrogen molecules at 300 K and 100 bar [165] and the numerical value is presented in Table 2. The total GHSC of each samples show the similar trend with the excess GHSC and the former of MC_5 exceeds the hydrogen storage performance of typical metal hydride, TiFe compound of 1.2 to 1.4 wt%[166]. Therefore, the N-doped porous carbon is expected to use in a specific application where the volumetric hydrogen storage capacity is not important.

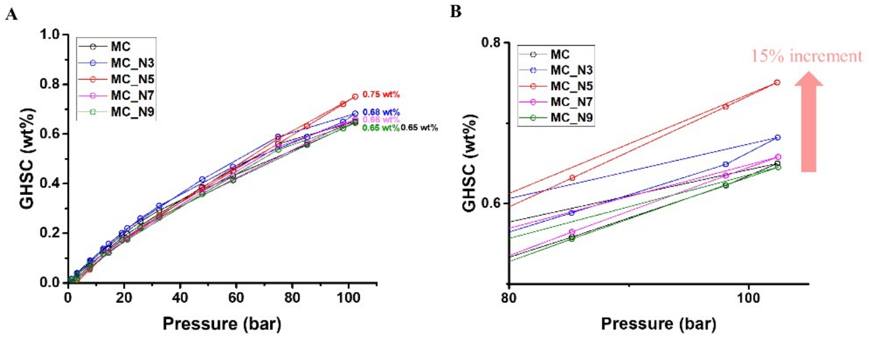

Figure 5.3. (A) GHSC of each sample, all of which are measured at 300 K and 100 bar (B) the enlarged figure to manifest the increment effect.

Table 5.2. Hydrogen storage performance of MC and N-doped MCs at 300 K and 100 bar

Sample code	**MC**	**MC_N3**	**MC_ N5**	**MC_ N7**	**MC_ N9**
Excess GHSC (wt%)	0.65	0.68	0.75	0.66	0.65
Total GHSC (wt%)	1.37	1.45	1.59	1.44	1.35

5.4. Conclusions

The effectiveness of sub-1nm nanopore and introduction of heteroatom on the modulation of IEMF was recently verified. We synthesized N-doped MCs containing large sub-1nm pore volume via nitrogen plasma treatment and confirmed the control of sub-1nm pore volume and N content simultaneously after nitrogen plasma treatment. The manifest increase of hydrogen storage performance of N-doped porous carbon is identified and nitrogen plasma-treated porous carbon for 5 min exhibits the best performance. For investigating its practicality, total GHSC of MC_N5 was calculated and the possibility of use in a specific application was confirmed by comparing the hydrogen storage performance of typical metal hydride system.

Part IV

Conclusions

Chapter 6. Concluding remarks and future plan.

While analyzing the previously reported hydrogen storage performance, the need for a new factor to explain the hydrogen storage phenomenon was found. I noted an eccentric phenomenon in carbon nanopores with a diameters of sub-1 nm and a hypothesis of hydrogen storage by intrinsic electromagnetic field was found to find out the underlying mechanism concerning the phenomenon. As a result, it was verified that this phenomenon is caused by the overlap of the IEMF of carbon walls and the resultant IEMF inside the carbon nanopore. Additionally, morphology-induced IEMF modulation thereby showing different hydrogen storage behavior is confirmed. Next, I raised questions about how to modulate the IEMF and what correlation between its modulation and hydrogen storage performance exists. To this end, the distribution of the IEMF direction and IEMF strength of bilayer graphene with different interlayer distances and different N contents were analyzed. For both cases, it is discovered that effective modulation of IEMF is possible and that the specific distribution of the IEMF only forms in the interlayer space. Additionally, it is verified that IEMF modulation is highly correlated to hydrogen storage performance and that the H_2 storage by the IEMF interaction is valid.

On that basis, N-doped microporous carbons containing large sub-1 nm pore volume via nitrogen plasma treatment were synthesized and their hydrogen storage performance were measured. While their effect on increasing hydrogen storage performance is manifest as shown in Figure 6.1., further work is required to reach D.O.E targets of hydrogen storage. To modulate IEMF of carbon nanopore, only nitrogen atoms were introduced in this research; however, much higher GHSC is predicted via introduction of various light heteroatoms (O, F etc.) into carbon nanopore, resulting in the maximizing E-IEMF well. Also, adopting established LNG tank system can be an easy way to commercializing hydrogen energy in terms of efficiency and economics given that rapid increases of hydrogen storage performance with lowering temperature are known and LNG tank is already operating at cryogenic temperature. Besides, the modulation of intrinsic magnetic field may be an effective to increase hydrogen storage performance because nuclear spin state of hydrogen molecules is changed at cryogenic temperature.

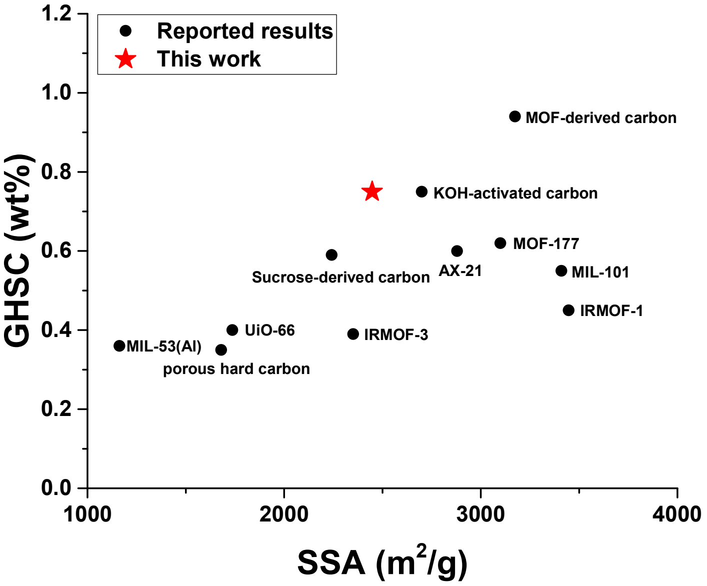

Figure 6.1. Comparison of GHSCs at 300 K and 100 bar of various porous materials already reported and plotted as a function of the SSA. Note the high performance of this work, given SSA.

Bibliography

1 Schlapbach, L. & Züttel, A. Hydrogen-storage materials for mobile applications. *Nature* 414, 353-358, doi:10.1038/35104634 (2001).

2 Durbin, D. J. & Malardier-Jugroot, C. Review of hydrogen storage techniques for on board vehicle applications. *International Journal of Hydrogen Energy* 38, 14595-14617, doi:10.1016/j.ijhydene.2013.07.058 (2013).

3 So, S. H., Sung, S. J., Yang, S. J. & Park, C. R. Where to go for the Development of High-Performance H2 Storage Materials at Ambient Conditions? *Electronic Materials Letters*, doi:10.1007/s13391-022-00368-2 (2022).

4 Rosi, N. L. *et al.* Hydrogen storage in microporous metal-organic frameworks. *Science* 300, 1127-1129, doi:10.1126/science.1083440 (2003).

5 Furukawa, H. & Yaghi, O. M. Storage of hydrogen, methane, and carbon dioxide in highly porous covalent organic frameworks for clean energy applications. *Journal of the American Chemical Society* 131, 8875-8883, doi:10.1021/ja9015765 (2009).

6 Yang, S. J. *et al.* MOF-derived hierarchically porous carbon with exceptional porosity and hydrogen storage capacity. *Chemistry of Materials* 24, 464-470 (2012).

7 Li, Y. & Yang, R. T. Gas adsorption and storage in metal-organic framework MOF-177. *Langmuir* 23, 12937-12944, doi:10.1021/la702466d (2007).

8 Farha, O. K. *et al.* De novo synthesis of a metal-organic framework material featuring ultrahigh surface area and gas storage capacities. *Nature Chemistry* 2, 944-948, doi:10.1038/nchem.834 (2010).

9 Latroche, M. *et al.* Hydrogen storage in the giant-pore metal-organic frameworks MIL-100 and MIL-101. *Angewandte Chemie - International Edition* 45, 8227-8231, doi:10.1002/anie.200600105 (2006).

10 Nishihara, H. *et al.* High-pressure hydrogen storage in zeolite-templated carbon. *Journal of Physical Chemistry C* **113**, 3189-3196, doi:10.1021/jp808890x (2009).

11 Yuan, D., Zhao, D., Sun, D. & Zhou, H. C. An isoreticular series of metal-organic frameworks with dendritic hexacarboxylate ligands and exceptionally high gas-uptake capacity. *Angewandte Chemie - International Edition* **49**, 5357-5361, doi:10.1002/anie.201001009 (2010).

12 Jordá-Beneyto, M., Suárez-García, F., Lozano-Castelló, D., Cazorla-Amorós, D. & Linares-Solano, A. Hydrogen storage on chemically activated carbons and carbon nanomaterials at high pressures. *Carbon* **45**, 293-303, doi:10.1016/j.carbon.2006.09.022 (2007).

13 Grochala, W. & Edwards, P. P. Thermal decomposition of the non-interstitial hydrides for the storage and production of hydrogen. *Chemical Reviews* **104**, 1283-1315, doi:10.1021/cr030691s (2004).

14 Orimo, S. I., Nakamori, Y., Eliseo, J. R., Züttel, A. & Jensen, C. M. Complex hydrides for hydrogen storage. *Chemical Reviews* **107**, 4111-4132, doi:10.1021/cr0501846 (2007).

15 Santos, D. M. F. & Sequeira, C. A. C. On the electrosynthesis of sodium borohydride. *International Journal of Hydrogen Energy* **35**, 9851-9861, doi:10.1016/j.ijhydene.2010.01.129 (2010).

16 Chen, P., Xiong, Z., Luo, J., Lin, J. & Lee Tan, K. Interaction of hydrogen with metal nitrides and imides. *Nature* **420**, 302-304, doi:10.1038/nature01210 (2002).

17 Stephens, F. H., Pons, V. & Baker, R. T. Ammonia-borane: The hydrogen source par excellence? *Dalton Transactions*, 2613-2626, doi:10.1039/b703053c (2007).

18 Biniwale, R. B., Rayalu, S., Devotta, S. & Ichikawa, M. Chemical hydrides: A solution to high capacity hydrogen storage and supply. *International Journal of Hydrogen Energy* **33**, 360-365, doi:10.1016/j.ijhydene.2007.07.028 (2008).

19 Zhu, Q. L. & Xu, Q. Liquid organic and inorganic chemical hydrides for high-capacity hydrogen storage. *Energy and Environmental Science* **8**, 478-512, doi:10.1039/c4ee03690e (2015).

20 Modisha, P. M., Ouma, C. N. M., Garidzirai, R., Wasserscheid, P. & Bessarabov, D. The Prospect of Hydrogen Storage Using Liquid Organic Hydrogen Carriers. *Energy and Fuels* **33**, 2778-2796, doi:10.1021/acs.energyfuels.9b00296 (2019).

21 Maurer, R. & Renken, A. Dehydrogenation of methanol to anhydrous formaldehyde in a microstuctured reactor system. *Chemical Engineering Research and Design* **81**, 730-734, doi:10.1205/026387603322302896 (2003).

22 Sakintuna, B., Lamari-Darkrim, F. & Hirscher, M. Metal hydride materials for solid hydrogen storage: A review. *International Journal of Hydrogen Energy* 32, 1121-1140, doi:10.1016/j.ijhydene.2006.11.022 (2007).

23 Reilly, J. J. & Wiswall, R. H. Formation and properties of iron titanium hydride. *Inorganic Chemistry* 13, 218-222, doi:10.1021/ic50131a042 (1974).

24 Sandrock, G. Panoramic overview of hydrogen storage alloys from a gas reaction point of view. *Journal of Alloys and Compounds* 293, 877-888, doi:10.1016/S0925-8388(99)00384-9 (1999).

25 Sujan, G. K., Pan, Z., Li, H., Liang, D. & Alam, N. An overview on TiFe intermetallic for solid-state hydrogen storage: microstructure, hydrogenation and fabrication processes. *Critical Reviews in Solid State and Materials Sciences* 45, 410-427, doi:10.1080/10408436.2019.1652143 (2020).

26 Dematteis, E. M. *et al.* Fundamental hydrogen storage properties of TiFe-alloy with partial substitution of Fe by Ti and Mn. *Journal of Alloys and Compounds* 874, doi:10.1016/j.jallcom.2021.159925 (2021).

27 Rusman, N. A. A. & Dahari, M. A review on the current progress of metal hydrides material for solid-state hydrogen storage applications. *International Journal of Hydrogen Energy* 41, 12108-12126, doi:10.1016/j.ijhydene.2016.05.244 (2016).

28 Pedziwiatr, A. T., Craig, R. S., Wallace, W. E. & Pourarian, F. Calorimetric enthalpies of formation and decomposition of hydrides of ZrMn2, ZrCr2, and related systems. *Journal of Solid State Chemistry* 46, 336-341, doi:10.1016/0022-4596(83)90158-5 (1983).

29 Liu, B. H., Kim, D. M., Lee, K. Y. & Lee, J. Y. Hydrogen storage properties of TiMn2-based alloys. *Journal of Alloys and Compounds* 240, 214-218, doi:10.1016/0925-8388(96)02245-1 (1996).

30 Pickering, L., Li, J., Reed, D., Bevan, A. I. & Book, D. Ti-V-Mn based metal hydrides for hydrogen storage. *Journal of Alloys and Compounds* 580, S233-S237, doi:10.1016/j.jallcom.2013.03.208 (2013).

31 Jung, J., Shin, B. S., Kang, J. W. & Han, W. S. Catalytic hydrogenation and dehydrogenation reactions of n-alkyl-bis(Carbazole)-based hydrogen storage materials. *Catalysts* 11, 1-10, doi:10.3390/catal11010123 (2021).

32 Crabtree, R. H. Hydrogen storage in liquid organic heterocycles. *Energy and Environmental Science* 1, 134-138, doi:10.1039/b805644g (2008).

33 Cui, Y. *et al.* The effect of substitution on the utility of piperidines and octahydroindoles for reversible hydrogen

storage. *New Journal of Chemistry* 32, 1027-1037, doi:10.1039/b718209k (2008).

34 Emel'Yanenko, V. N. *et al.* Hydrogen Storage: Thermochemical Studies of N-Alkylcarbazoles and Their Derivatives as a Potential Liquid Organic Hydrogen Carriers. *Journal of Physical Chemistry C* 119, 26381-26389, doi:10.1021/acs.jpcc.5b10392 (2015).

35 Rao, P. C. & Yoon, M. Potential liquid-organic hydrogen carrier (Lohc) systems: A review on recent progress. *Energies* 13, doi:10.3390/en13226040 (2020).

36 Liang, G., Huot, J., Boily, S., Van Neste, A. & Schulz, R. Catalytic effect of transition metals on hydrogen sorption in nanocrystalline ball milled MgH2-Tm (Tm = Ti, V, Mn, Fe and Ni) systems. *Journal of Alloys and Compounds* 292, 247-252, doi:10.1016/S0925-8388(99)00442-9 (1999).

37 Wagemans, R. W. P., Van Lenthe, J. H., De Jongh, P. E., Van Dillen, A. J. & De Jong, K. P. Hydrogen storage in magnesium clusters: Quantum chemical study. *Journal of the American Chemical Society* 127, 16675-16680, doi:10.1021/ja054569h (2005).

38 Li, W., Li, C., Ma, H. & Chen, J. Magnesium nanowires: Enhanced kinetics for hydrogen absorption and desorption. *Journal of the American Chemical Society* 129, 6710-6711, doi:10.1021/ja071323z (2007).

39 Zhang, X. *et al.* Realizing 6.7 wt% reversible storage of hydrogen at ambient temperature with non-confined ultrafine magnesium hydrides. *Energy and Environmental Science* 14, 2302-2313, doi:10.1039/d0ee03160g (2021).

40 Yang, S. J., Cho, J. H., Oh, G. H., Nahm, K. S. & Park, C. R. Easy synthesis of highly nitrogen-enriched graphitic carbon with a high hydrogen storage capacity at room temperature. *Carbon* 47, 1585-1591, doi:10.1016/j.carbon.2009.02.010 (2009).

41 Kang, K. Y., Lee, B. I. & Lee, J. S. Hydrogen adsorption on nitrogen-doped carbon xerogels. *Carbon* 47, 1171-1180, doi:10.1016/j.carbon.2009.01.001 (2009).

42 Wu, S., Fan, K., Wu, M. & Yin, G. Effect of nitrogen doping and external electric field on the adsorption of hydrogen on graphene. *EPJ Applied Physics* 75, doi:10.1051/epjap/2016160059 (2016).

43 Xia, Y., Walker, G. S., Grant, D. M. & Mokaya, R. Hydrogen storage in high surface area carbons: Experimental demonstration of the effects of nitrogen doping. *Journal of the American Chemical Society* 131, 16493-16499, doi:10.1021/ja9054838 (2009).

44 Wang, L. & Yang, R. T. Hydrogen storage properties of N-doped microporous carbon. *Journal of Physical Chemistry C* 113, 21883-21888, doi:10.1021/jp908156v (2009).

45 Chung, T. C. M., Jeong, Y., Chen, Q., Kleinhammes, A. & Wu, Y. Synthesis of microporous boron-substituted carbon (B/C) materials using polymeric precursors for hydrogen physisorption. *Journal of the American Chemical Society* 130, 6668-6669, doi:10.1021/ja800071y (2008).

46 Jeong, Y. & Mike Chung, T. C. The synthesis and characterization of a super-activated carbon containing substitutional boron (BCx) and its applications in hydrogen storage. *Carbon* 48, 2526-2537, doi:10.1016/j.carbon.2010.03.029 (2010).

47 Sathishkumar, N., Wu, S. Y. & Chen, H. T. Boron- and nitrogen-doped penta-graphene as a promising material for hydrogen storage: A computational study. *International Journal of Energy Research* 43, 4867-4878, doi:10.1002/er.4639 (2019).

48 Hu, W. *et al.* Sodium alginate assisted preparation of oxygen-doped microporous carbons with enhanced electrochemical energy storage and hydrogen uptake. *International Journal of Hydrogen Energy* 46, 896-905, doi:10.1016/j.ijhydene.2020.09.232 (2021).

49 Tellez-Juárez, M. C. *et al.* Hydrogen storage in activated carbons produced from coals of different ranks: Effect of oxygen content. *International Journal of Hydrogen Energy* 39, 4996-5002, doi:10.1016/j.ijhydene.2014.01.071 (2014).

50 Georgakis, M., Stavropoulos, G. & Sakellaropoulos, G. P. Molecular dynamics study of hydrogen adsorption in carbonaceous microporous materials and the effect of oxygen functional groups. *International Journal of Hydrogen Energy* 32, 1999-2004, doi:10.1016/j.ijhydene.2006.08.040 (2007).

51 Blankenship, T. S., Balahmar, N. & Mokaya, R. Oxygen-rich microporous carbons with exceptional hydrogen storage capacity. *Nature Communications* 8, doi:10.1038/s41467-017-01633-x (2017).

52 Jiang, J., Gao, Q., Zheng, Z., Xia, K. & Hu, J. Enhanced room temperature hydrogen storage capacity of hollow nitrogen-containing carbon spheres. *International Journal of Hydrogen Energy* 35, 210-216, doi:10.1016/j.ijhydene.2009.10.042 (2010).

53 Jhi, S. H. & Kwon, Y. K. Hydrogen adsorption on boron nitride nanotubes: A path to room-temperature hydrogen storage. *Physical Review B - Condensed Matter and Materials Physics* 69, 245407-245401-245407-245404, doi:10.1103/PhysRevB.69.245407 (2004).

54 Mpourmpakis, G. & Froudakis, G. E. Why boron nitride nanotubes are preferable to carbon nanotubes for hydrogen storage?. An ab initio theoretical study. *Catalysis Today* **120**, 341-345, doi:10.1016/j.cattod.2006.09.023 (2007).

55 Ma, R. *et al.* Hydrogen uptake in boron nitride nanotubes at room temperature. *Journal of the American Chemical Society* **124**, 7672-7673, doi:10.1021/ja026030e (2002).

56 Leela Mohana Reddy, A., Tanur, A. E. & Walker, G. C. Synthesis and hydrogen storage properties of different types of boron nitride nanostructures. *International Journal of Hydrogen Energy* **35**, 4138-4143, doi:10.1016/j.ijhydene.2010.01.072 (2010).

57 Li, J. *et al.* Porous boron nitride with a high surface area: Hydrogen storage and water treatment. *Nanotechnology* **24**, doi:10.1088/0957-4484/24/15/155603 (2013).

58 Lian, G. *et al.* Controlled fabrication of ultrathin-shell BN hollow spheres with excellent performance in hydrogen storage and wastewater treatment. *Energy and Environmental Science* **5**, 7072-7080, doi:10.1039/c2ee03240f (2012).

59 Stephan, D. W. & Erker, G. Frustrated lewis pairs: metal-free hydrogen activation and more. *Angewandte Chemie - International Edition* **49**, 46-76, doi:10.1002/anie.200903708 (2010).

60 Mao, H., Chen, Z., Cheng, L. & Wang, K. The activity and reversibility of intramolecular B/N Frustrated Lewis Pairs in the hydrogenation. *International Journal of Hydrogen Energy* **46**, 110-118, doi:10.1016/j.ijhydene.2020.09.248 (2021).

61 Heshmat, M. & Ensing, B. Optimizing the Energetics of FLP-Type H2Activation by Modulating the Electronic and Structural Properties of the Lewis Acids: A DFT Study. *Journal of Physical Chemistry A* **124**, 6399-6410, doi:10.1021/acs.jpca.0c03108 (2020).

62 Ma, G., Song, G. & Li, Z. H. Designing Metal-Free Frustrated Lewis Pairs Catalyst for the Efficient Dehydrogenation of Ammonia Borane. *Chemistry - A European Journal* **24**, 13238-13245, doi:10.1002/chem.201801932 (2018).

63 Stephan, D. W. The broadening reach of frustrated Lewis pair chemistry. *Science* **354**, doi:10.1126/science.aaf7229 (2016).

64 Welch, G. C., San Juan, R. R., Masuda, J. D. & Stephan, D. W. Reversible, metal-free hydrogen activation. *Science* **314**, 1124-1126, doi:10.1126/science.1134230 (2006).

65 Suh, M. P., Park, H. J., Prasad, T. K. & Lim, D. W. Hydrogen storage in metal-organic frameworks. *Chemical Reviews* **112**, 782-835, doi:10.1021/cr200274s (2012).

66 Dinča, M. *et al.* Hydrogen storage in a microporous metal-organic framework with exposed Mn2+ coordination sites.

Journal of the American Chemical Society 128, 16876-16883, doi:10.1021/ja0656853 (2006).

67 Kim, T. K. & Suh, M. P. Selective CO2 adsorption in a flexible non-interpenetrated metal-organic framework. *Chemical Communications* 47, 4258-4260, doi:10.1039/c0cc05199c (2011).

68 Jaramillo, D. E. *et al.* Ambient-Temperature Hydrogen Storage via Vanadium(II)-Dihydrogen Complexation in a Metal-Organic Framework. *Journal of the American Chemical Society* 143, 6248-6256, doi:10.1021/jacs.1c01883 (2021).

69 Gallego, N. C., He, L., Saha, D., Contescu, C. I. & Melnichenko, Y. B. Hydrogen confinement in carbon nanopores: Extreme densification at ambient temperature. *Journal of the American Chemical Society* 133, 13794-13797, doi:10.1021/ja202432x (2011).

70 Kowalczyk, P., Hołyst, R., Terzyk, A. P. & Gauden, P. A. State of hydrogen in idealized carbon slitlike nanopores at 77 K. *Langmuir* 22, 1970-1972, doi:10.1021/la053041n (2006).

71 Masika, E. & Mokaya, R. Hydrogen storage in high surface area carbons with identical surface areas but different pore sizes: Direct demonstration of the effects of pore size. *Journal of Physical Chemistry C* 116, 25734-25740, doi:10.1021/jp3100365 (2012).

72 Patchkovskii, S. *et al.* Graphene nanostructures as tunable storage media for molecular hydrogen. *Proceedings of the National Academy of Sciences of the United States of America* 102, 10439-10444, doi:10.1073/pnas.0501030102 (2005).

73 Liu, S. *et al.* Hydrogen storage in incompletely etched multilayer Ti2CTx at room temperature. *Nature Nanotechnology* 16, 331-336, doi:10.1038/s41565-020-00818-8 (2021).

74 Gogotsi, Y. *et al.* Tailoring of nanoscale porosity in carbide-derived carbons for hydrogen storage. *Journal of the American Chemical Society* 127, 16006-16007, doi:10.1021/ja0550529 (2005).

75 Cabria, I., López, M. J. & Alonso, J. A. The optimum average nanopore size for hydrogen storage in carbon nanoporous materials. *Carbon* 45, 2649-2658, doi:10.1016/j.carbon.2007.08.003 (2007).

76 Yang, S. J. *et al.* General relationship between hydrogen adsorption capacities at 77 and 298 K and pore characteristics of the porous adsorbents. *Journal of Physical Chemistry C* 116, 10529-10540, doi:10.1021/jp302304w (2012).

77 Kim, B. H. *et al.* Thermally modulated multilayered graphene oxide for hydrogen storage. *Physical Chemistry Chemical Physics* 14, 1480-1484, doi:10.1039/c2cp23683d (2012).

78 Chung, C. H., Ihm, J. & Lee, H. Recent progress on Kubas-type hydrogen-storage nanomaterials: from theories to experiments. *Journal of the Korean Physical Society* 66, 1649-1655, doi:10.3938/jkps.66.1649 (2015).

79 Skipper, C. V. J., Hamaed, A., Antonelli, D. M. & Kaltsoyannis, N. The Kubas interaction in M(ii) (M = Ti, V, Cr) hydrazine-based hydrogen storage materials: A DFT study. *Dalton Transactions* 41, 8515-8523, doi:10.1039/c2dt30383c (2012).

80 Skipper, C. V. J., Hamaed, A., Antonelli, D. M. & Kaltsoyannis, N. Computational study of silica-supported transition metal fragments for Kubas-type hydrogen storage. *Journal of the American Chemical Society* 132, 17296-17305, doi:10.1021/ja107539j (2010).

81 Hoang, T. K. A. *et al.* Kubas-type hydrogen storage in V(III) polymers using tri- and tetradentate bridging ligands. *Journal of the American Chemical Society* 133, 4955-4964, doi:10.1021/ja110243r (2011).

82 Hamaed, A. *et al.* Hydride-induced amplification of performance and binding enthalpies in chromium hydrazide gels for Kubas-type hydrogen storage. *Journal of the American Chemical Society* 133, 15434-15443, doi:10.1021/ja2021944 (2011).

83 Hoang, T. K. A., Morris, L., Rawson, J. M., Trudeau, M. L. & Antonelli, D. M. Multivalent manganese hydrazide gels for kubas-type hydrogen storage. *Chemistry of Materials* 24, 1629-1638, doi:10.1021/cm300425z (2012).

84 Kim, Y. H., Zhao, Y., Williamson, A., Heben, M. J. & Zhang, S. B. Nondissociative adsorption of H2 molecules in light-element-doped fullerenes. *Physical Review Letters* 96, doi:10.1103/PhysRevLett.96.016102 (2006).

85 Hamaed, A., Trudeau, M. & Antonelli, D. M. H2 storage materials (22KJ/mol) using organometallic Ti fragments as σ-H2 binding sites. *Journal of the American Chemical Society* 130, 6992-6999, doi:10.1021/ja710288g (2008).

86 Morris, L., Trudeau, M. L., Reed, D., Book, D. & Antonelli, D. M. High-Pressure Raman and Calorimetry Studies of Vanadium(III) Alkyl Hydrides for Kubas-Type Hydrogen Storage. *ChemPhysChem* 17, 822-828, doi:10.1002/cphc.201501093 (2016).

87 Park, N. *et al.* Progress on first-principles-based materials design for hydrogen storage. *Proceedings of the National Academy of Sciences of the United States of America* 109, 19893-19899, doi:10.1073/pnas.1217137109 (2012).

88 Khoobiar, S. Particle to particle migration of hydrogen atoms on platinum-alumina catalysts from particle to neighboring

particles. *Journal of Physical Chemistry* 68, 411-412, doi:10.1021/j100784a503 (1964).

89 Karim, W. *et al.* Catalyst support effects on hydrogen spillover. *Nature* 541, 68-71, doi:10.1038/nature20782 (2017).

90 Li, Y. & Yang, R. T. Significantly enhanced hydrogen storage in metal-organic frameworks via spillover. *Journal of the American Chemical Society* 128, 726-727, doi:10.1021/ja056831s (2006).

91 Wang, L. & Yang, R. T. Hydrogen storage properties of carbons doped with ruthenium, platinum, and nickel nanoparticles. *Journal of Physical Chemistry C* 112, 12486-12494, doi:10.1021/jp803093w (2008).

92 Li, Y. & Yang, R. T. Hydrogen storage in low silica type X zeolites. *Journal of Physical Chemistry B* 110, 17175-17181, doi:10.1021/jp0634508 (2006).

93 Li, Y. & Yang, R. T. Hydrogen storage on platinum nanoparticles doped on superactivated carbon. *Journal of Physical Chemistry C* 111, 11086-11094, doi:10.1021/jp072867q (2007).

94 Yang, F. H., Lachawiec Jr, A. J. & Yang, R. T. Adsorption of spillover hydrogen atoms on single-wall carbon nanotubes. *Journal of Physical Chemistry B* 110, 6236-6244, doi:10.1021/jp056461u (2006).

95 Wang, L. & Yang, R. T. Hydrogen storage on carbon-based adsorbents and storage at ambient temperature by hydrogen spillover. *Catalysis Reviews - Science and Engineering* 52, 411-461, doi:10.1080/01614940.2010.520265 (2010).

96 Wang, L., Stuckert, N. R., Chen, H. & Yang, R. T. Effects of Pt particle size on hydrogen storage on Pt-doped metal-organic framework IRMOF-8. *Journal of Physical Chemistry C* 115, 4793-4799, doi:10.1021/jp111800c (2011).

97 Stuckert, N. R., Wang, L. & Yang, R. T. Characteristics of hydrogen storage by spillover on Pt-doped carbon and catalyst-bridged metal organic framework. *Langmuir* 26, 11963-11971, doi:10.1021/la101377u (2010).

98 Yang, R. T. & Wang, Y. Catalyzed hydrogen spillover for hydrogen storage. *Journal of the American Chemical Society* 131, 4224-4226, doi:10.1021/ja808864r (2009).

99 Wang, Z., Yang, F. H. & Yang, R. T. Enhanced hydrogen spillover on carbon surfaces modified by oxygen plasma. *Journal of Physical Chemistry C* 114, 1601-1609, doi:10.1021/jp909480d (2010).

100 Wang, L. & Yang, R. T. New sorbents for hydrogen storage by hydrogen spillover - A review. *Energy and Environmental Science* 1, 268-279, doi:10.1039/b807957a (2008).

101 Li, Y. & Yang, R. T. Hydrogen storage in metal-organic frameworks by bridged hydrogen spillover. *Journal of the American Chemical Society* 128, 8136-8137, doi:10.1021/ja061681m (2006).

102 Campesi, R., Cuevas, F., Latroche, M. & Hirscher, M. Hydrogen spillover measurements of unbridged and bridged metal-organic frameworks - Revisited. *Physical Chemistry Chemical Physics* 12, 10457-10459, doi:10.1039/c0cp00037j (2010).

103 Stadie, N. P., Purewal, J. J., Ahn, C. C. & Fultz, B. Measurements of hydrogen spillover in platinum doped superactivated carbon. *Langmuir* 26, 15481-15485, doi:10.1021/la9046758 (2010).

104 Oh, H. *et al.* Hydrogen adsorption properties of platinum decorated hierarchically structured templated carbons. *Microporous and Mesoporous Materials* 177, 66-74, doi:10.1016/j.micromeso.2013.04.020 (2013).

105 Yi, D. *et al.* Emergent electric field control of phase transformation in oxide superlattices. *Nature Communications* 11, doi:10.1038/s41467-020-14631-3 (2020).

106 Asamitsu, A., Moritomo, Y., Tomioka, Y., Arimat, T. & Tokura, Y. A structural phase transition induced by an external magnetic field. *Nature* 373, 407-409, doi:10.1038/373407a0 (1995).

107 Kuwahara, H., Tomioka, Y., Asamitsu, A., Moritomo, Y. & Tokura, Y. A first-order phase transition induced by a magnetic field. *Science* 270, 961-963, doi:10.1126/science.270.5238.961 (1995).

108 Yethiraj, A., Wouterse, A., Groh, B. & Van Blaaderen, A. Nature of an Electric-Field-Induced Colloidal Martensitic Transition. *Physical Review Letters* 92, 583011-583014 (2004).

109 Hirotsu, S. Electric-field-induced phase transition in polymer gels. *Japanese Journal of Applied Physics* 24, 396-388, doi:10.7567/JJAPS.24S2.396 (1985).

110 Nazir, G. *et al.* Recent Advances and Reliable Assessment of Solid-State Materials for Hydrogen Storage: A Step Forward toward a Sustainable H2 Economy. *Advanced Sustainable Systems* 6, doi:10.1002/adsu.202200276 (2022).

111 Boddien, A. & Junge, H. Catalysis: Acidic ideas for hydrogen storage. *Nature Nanotechnology* 6, 265-266, doi:10.1038/nnano.2011.70 (2011).

112 Schlapbach, L. Technology: Hydrogen-fuelled vehicles. *Nature* 460, 809-811, doi:10.1038/460809a (2009).

113 Nazir, G. *et al.* Heteroatoms-doped hierarchical porous carbons: Multifunctional materials for effective methylene blue

removal and cryogenic hydrogen storage. *Colloids and Surfaces A: Physicochemical and Engineering Aspects* 630, doi:10.1016/j.colsurfa.2021.127554 (2021).

114 Ahmed, A. *et al.* Exceptional hydrogen storage achieved by screening nearly half a million metal-organic frameworks. *Nature Communications* 10, doi:10.1038/s41467-019-09365-w (2019).

115 Ahmed, A. *et al.* Balancing gravimetric and volumetric hydrogen density in MOFs. *Energy and Environmental Science* 10, 2459-2471, doi:10.1039/c7ee02477k (2017).

116 Yang, J., Sudik, A., Wolverton, C. & Siegel, D. J. High capacity hydrogen storage materials: Attributes for automotive applications and techniques for materials discovery. *Chemical Society Reviews* 39, 656-675, doi:10.1039/b802882f (2010).

117 Sang, S. H., Furukawa, H., Yaghi, O. M. & Goddard Iii, W. A. Covalent organic frameworks as exceptional hydrogen storage materials. *Journal of the American Chemical Society* 130, 11580-11581, doi:10.1021/ja803247y (2008).

118 Cao, D., Lan, J., Wang, W. & Smit, B. Lithium-doped 3D covalent organic frameworks: High-capacity hydrogen storage materials. *Angewandte Chemie - International Edition* 48, 4730-4733, doi:10.1002/anie.200900960 (2009).

119 Ding, S. Y. & Wang, W. Covalent organic frameworks (COFs): From design to applications. *Chemical Society Reviews* 42, 548-568, doi:10.1039/c2cs35072f (2013).

120 Lee, S. Y., Park, J. H., Heo, Y. J., Lee, E. S. & Park, S. J. A study on electron acceptor of carbonaceous materials for highly efficient hydrogen uptakes. *Catalysts* 11, doi:10.3390/catal11121524 (2021).

121 Goldsmith, J., Wong-Foy, A. G., Cafarella, M. J. & Siegel, D. J. Theoretical limits of hydrogen storage in metal-organic frameworks: Opportunities and trade-offs. *Chemistry of Materials* 25, 3373-3382, doi:10.1021/cm401978e (2013).

122 Xia, K., Gao, Q., Wu, C., Song, S. & Ruan, M. Activation, characterization and hydrogen storage properties of the mesoporous carbon CMK-3. *Carbon* 45, 1989-1996, doi:10.1016/j.carbon.2007.06.002 (2007).

123 Cho, E. S. *et al.* Graphene oxide/metal nanocrystal multilaminates as the atomic limit for safe and selective hydrogen storage. *Nature Communications* 7, doi:10.1038/ncomms10804 (2016).

124 So, S. H. *et al.* Demonstration of the nanosize effect of carbon nanomaterials on the dehydrogenation temperature of ammonia borane. *Nanoscale Advances* 1, 4697-4703, doi:10.1039/c9na00501c (2019).

125 Ting, V. P. *et al.* Direct Evidence for Solid-like Hydrogen in a Nanoporous Carbon Hydrogen Storage Material at Supercritical Temperatures. *ACS Nano* 9, 8249-8254, doi:10.1021/acsnano.5b02623 (2015).

126 Tian, M. *et al.* Effect of pore geometry on ultra-densified hydrogen in microporous carbons. *Carbon* 173, 968-979, doi:10.1016/j.carbon.2020.11.063 (2021).

127 Olsen, R. J. *et al.* Phase Transition of H2 in Subnanometer Pores Observed at 75 K. *ACS Nano* 11, 11617-11631, doi:10.1021/acsnano.7b06640 (2017).

128 Tunuguntla, R. H., Allen, F. I., Kim, K., Belliveau, A. & Noy, A. Ultrafast proton transport in sub-1-nm diameter carbon nanotube porins. *Nature Nanotechnology* 11, 639-644, doi:10.1038/nnano.2016.43 (2016).

129 Chmiola, J. *et al.* Anomalous increase in carbon at pore sizes less than 1 nanometer. *Science* 313, 1760-1763, doi:10.1126/science.1132195 (2006).

130 Koga, K., Gao, G. T., Tanaka, H. & Zeng, X. C. Formation of ordered ice nanotubes inside carbon nanotubes. *Nature* 412, 802-805, doi:10.1038/35090532 (2001).

131 Espinosa-Ortega, T., Luk'Yanchuk, I. A. & Rubo, Y. G. Magnetic properties of graphene quantum dots. *Physical Review B - Condensed Matter and Materials Physics* 87, doi:10.1103/PhysRevB.87.205434 (2013).

132 Ominato, Y. & Koshino, M. Orbital magnetism of graphene flakes. *Physical Review B - Condensed Matter and Materials Physics* 87, doi:10.1103/PhysRevB.87.115433 (2013).

133 Ominato, Y. & Koshino, M. Orbital magnetic susceptibility of finite-sized graphene. *Physical Review B - Condensed Matter and Materials Physics* 85, doi:10.1103/PhysRevB.85.165454 (2012).

134 Hoyland, J. R. Magnetic and electrical properties of small diatomic molecules. i. diamagnetic susceptibility, proton-shielding constant, and electric polarizability of the hydrogen molecule. *The Journal of Chemical Physics* 41, 3153-3158, doi:10.1063/1.1725689 (1964).

135 Kołos, W. & Wolniewicz, L. Polarizability of the hydrogen molecule. *The Journal of Chemical Physics* 46, 1426-1432, doi:10.1063/1.1840870 (1967).

136 Sun, D., Zhang, Y. P., Wei, X. J., Wang, L. M. & Yan, Z. C. Polarizabilities of hydrogen molecules calculated without using the Born-Oppenheimer approximation. *Physical Review A* 103, doi:10.1103/PhysRevA.103.062813 (2021).

137 Wilkins, R. L. & Taylor, H. S. Polarizability of molecular hydrogen. *The Journal of Chemical Physics* 48, 4934-4937, doi:10.1063/1.1668159 (1968).

138 Scuseria, G. E., Miller, M. D., Jensen, F. & Geertsen, J. The dipole moment of carbon monoxide. *The Journal of Chemical Physics* 94, 6660-6663, doi:10.1063/1.460293 (1991).

139 Yamato, M. & Kimura, T. Magnetic processing of diamagnetic materials. *Polymers* 12, 1-23, doi:10.3390/polym12071491 (2020).

140 Silvera, I. F. The solid molecular hydrogens in the condensed phase: Fundamentals and static properties. *Reviews of Modern Physics* 52, 393-452, doi:10.1103/RevModPhys.52.393 (1980).

141 Sun, Q., Wang, Q., Jena, P. & Kawazoe, Y. Clustering of Ti on a C60 surface and its effect on hydrogen storage. *Journal of the American Chemical Society* 127, 14582-14583, doi:10.1021/ja0550125 (2005).

142 Zhao, Y., Kim, Y. H., Dillon, A. C., Heben, M. J. & Zhang, S. B. Hydrogen storage in novel organometallic buckyballs. *Physical Review Letters* 94, doi:10.1103/PhysRevLett.94.155504 (2005).

143 Singh, A. K., Sadrzadeh, A. & Yakobson, B. I. Metallacarboranes: Toward promising hydrogen storage metal organic frameworks. *Journal of the American Chemical Society* 132, 14126-14129, doi:10.1021/ja104544s (2010).

144 Mpourmpakis, G., Froudakis, G. E., Lithoxoos, G. P. & Samios, J. SiC nnotubes: A novel material for hydrogen storage. *Nano Letters* 6, 1581-1583, doi:10.1021/nl0603911 (2006).

145 He, T., Pachfule, P., Wu, H., Xu, Q. & Chen, P. Hydrogen carriers. *Nature Reviews Materials* 1, doi:10.1038/natrevmats.2016.59 (2016).

146 Shao, H., Xin, G., Zheng, J., Li, X. & Akiba, E. Nanotechnology in Mg-based materials for hydrogen storage. *Nano Energy* 1, 590-601, doi:10.1016/j.nanoen.2012.05.005 (2012).

147 Kim, T. H. *et al.* Room-temperature hydrogen storage via two-dimensional potential well in mesoporous graphene oxide. *Nano Energy* 27, 402-411, doi:10.1016/j.nanoen.2016.07.027 (2016).

148 Thornton, A. W., Nairn, K. M., Hill, J. M., Hill, A. J. & Hill, M. R. Metal-organic frameworks impregnated with magnesium-decorated fullerenes for methane and hydrogen storage. *Journal of the American Chemical Society* 131, 10662-10669, doi:10.1021/ja9036302 (2009).

149 Gogotsi, Y. *et al.* Importance of pore size in high-pressure hydrogen storage by porous carbons. *International Journal of Hydrogen Energy* 34, 6314-6319, doi:10.1016/j.ijhydene.2009.05.073 (2009).

150 Yushin, G., Dash, R., Jagiello, J., Fischer, J. E. & Gogotsi, Y. Carbide-derived carbons: Effect of pore size on hydrogen uptake and heat of adsorption. *Adv. Funct. Mater.* 16, 2288-2293, doi:10.1002/adfm.200500830 (2006).

151 Sevilla, M., Fuertes, A. B. & Mokaya, R. High density hydrogen storage in superactivated carbons from hydrothermally carbonized renewable organic materials. *Energy and Environmental Science* 4, 1400-1410, doi:10.1039/c0ee00347f (2011).

152 Yang, Z., Xia, Y. & Mokaya, R. Enhanced hydrogen storage capacity of high surface area zeolite-like carbon materials. *Journal of the American Chemical Society* 129, 1673-1679, doi:10.1021/ja067149g (2007).

153 Sevilla, M., Mokaya, R. & Fuertes, A. B. Ultrahigh surface area polypyrrole-based carbons with superior performance for hydrogen storage. *Energy and Environmental Science* 4, 2930-2936, doi:10.1039/c1ee01608c (2011).

154 Srinivas, G., Burress, J. W., Ford, J. & Yildirim, T. Porous graphene oxide frameworks: Synthesis and gas sorption properties. *Journal of Materials Chemistry* 21, 11323-11329, doi:10.1039/c1jm11699a (2011).

155 Zhang, H. P., Luo, X. G., Lin, X. Y., Lu, X. & Leng, Y. Density functional theory calculations of hydrogen adsorption on Ti-, Zn-, Zr-, Al-, and N-doped and intrinsic graphene sheets. *International Journal of Hydrogen Energy* 38, 14269-14275, doi:10.1016/j.ijhydene.2013.07.098 (2013).

156 Petrushenko, I. K. & Petrushenko, K. B. Hydrogen physisorption on nitrogen-doped graphene and graphene-like boron nitride-carbon heterostructures: a DFT study. *Surfaces and Interfaces* 17, doi:10.1016/j.surfin.2019.100355 (2019).

157 Ito, Y. *et al.* Tuning the Magnetic Properties of Carbon by Nitrogen Doping of Its Graphene Domains. *Journal of the American Chemical Society* 137, 7678-7685, doi:10.1021/ja512897m (2015).

158 Błoński, P. *et al.* Doping with Graphitic Nitrogen Triggers Ferromagnetism in Graphene. *Journal of the American Chemical Society* 139, 3171-3180, doi:10.1021/jacs.6b12934 (2017).

159 Yang, S. J. *et al.* A sustainable synthesis alternative for IL-derived N-doped carbons: Bio-based-imidazolium compounds. *Carbon* 94, 641-645, doi:10.1016/j.carbon.2015.07.034 (2015).

160 Kajiura, H. *et al.* Hydrogen storage capacity of commercially available carbon materials at room temperature. *Applied Physics Letters* 82, 1105-1107, doi:10.1063/1.1555262 (2003).

161 Xia, Y., Yang, Z. & Zhu, Y. Porous carbon-based materials for hydrogen storage: Advancement and challenges. *Journal of Materials Chemistry A* 1, 9365-9381, doi:10.1039/c3ta10583k (2013).

162 Sevilla, M. & Mokaya, R. Energy storage applications of activated carbons: Supercapacitors and hydrogen storage.

Energy and Environmental Science 7, 1250-1280, doi:10.1039/c3ee43525c (2014).

163 Lim, C., Kwak, C. H., Jeong, S. G., Kim, D. & Lee, Y. S. Enhanced CO2 adsorption of activated carbon with simultaneous surface etching and functionalization by nitrogen plasma treatment. *Carbon Letters*, doi:10.1007/s42823-022-00410-1 (2022).

164 Lin, X. *et al.* High capacity hydrogen adsorption in Cu(II) tetracarboxylate framework materials: The role of pore size, ligand functionalization, and exposed metal sites. *Journal of the American Chemical Society* 131, 2159-2171, doi:10.1021/ja806624j (2009).

165 Kaye, S. S., Dailly, A., Yaghi, O. M. & Long, J. R. Impact of preparation and handling on the hydrogen storage properties of Zn4O(1,4-benzenedicarboxylate)3 (MOF-5). *Journal of the American Chemical Society* 129, 14176-14177, doi:10.1021/ja076877g (2007).

166 Padhee, S. P., Roy, A. & Pati, S. Role of Mn-substitution towards the enhanced hydrogen storage performance in FeTi. *International Journal of Hydrogen Energy* 47, 9357-9371, doi:10.1016/j.ijhydene.2022.01.032 (2022).

국문 초록

유망한 재생에너지인 수소 에너지를 상용화하기 위해서는 안전하고 많은 양의 수소를 저장, 이송할 수 있는 기술이 시급히 개발되어야 한다. 현재 상용화를 목적으로 고려되고 있는 압축 방식과 액화 방식은 고압으로 인한 안정성 문제와 외부 열 유입에 의한 boil-off 문제를 해결하지 못하고 있는 실정이다. 이에 대한 하나의 대안 기술로 흡착현상을 이용한 수소저장 연구가 많이 이루어졌지만 아직까지는 대안으로서의 가능성은 보여주지 못하고 있다. 그러나 다수의 선행연구에서는 특정 크기의 나노 기공 조건에서 액체 수소의 밀도를 보이는 고밀도 수소저장이 가능함을 보고하고 있다. 따라서 이 연구에서는 그러한 고밀도 수소저장이 가능한 원인을 규명하여 상온에서도 고밀도 수소 저장을 할 수 있는 수소저장재 개발의 과학기술적 가이드라인을 제시하고자 한다. Part 1 에서는 수소 저장 분야에 관해 전반적인 소개와 심층적인 수소저장 메커니즘 규명의 필요성을 강조하였다. Part 2 에서는 내재적 전자기장에 의한 수소저장이라는 가설을 검증하는 연구를 수행하였다. 몰폴로지, 기공 크기, 원자 조성에 따라 내재적 전자기장이 유의미하게 변조되었고, 이는 수소저장성능과 밀접한 상관성이 있음을 보였다. Part 3 에서는 앞서 검증된 가설을

바탕으로 질소 플라즈마 처리를 통해 직경 1 nm 미만 기공 부피와 질소 함량을 동시에 증가시킴으로써 소재의 상온 수소저장성능을 증대시킨 연구 결과를 제시하였다. 이 연구는 직경 1nm 미만 탄소나노기공에서 발생하는 특이한 현상뿐만 아니라 호스트-게스트 상호작용 개념을 포괄하기 때문에 결과적으로 다른 연구 분야(예: 슈퍼커패시터, 배터리, 촉매)에 대한 새로운 통찰력을 제공할 수 있을 것으로 기대된다.

감사의 말씀

본인에게 박사 학위 과정을 마무리할 수 있는 날이 올 수 있을지에 대한 의구심을 품으면서 하루하루 연구실 생활을 해 왔었는데 결실을 맺어보니 어안이 벙벙합니다. 박사 학위 기간 동안 셀 수 없는 소중한 것들을 손에 쥘 수 있어서 너무 기쁩니다. 첫째로 자기 생각이 강했던 본인이 부모님의 사랑을 알아들을 수 있는 청력을 가지게 된 점입니다. 둘째로 지도 교수님께서 열과 성의를 다해 포기하지 않고 지도 학생들에게 전해주고 싶어하셨던 연구 철학을 이해하게 되면서 연구관이 확립될 수 있었을 뿐만 아니라 세계관을 대폭 넓힐 수 있었던 점입니다. 셋째로 철없는 저를 옆에서 끝까지 응원해 주었던 서울대학교 선배들과 친구들을 지인으로 삼고 그들에게 배울 수 있는 기회를 얻었던 점입니다. 글솜씨가 부족해서 하고 싶은 말을 전달력 있게 쓰지 못하였지만 자랑스러운 대한민국에 수소에너지를 하루 빨리 보급시키는데 힘씀으로써 세상을 아름답게 하고 감사했던 분들께 은혜를 갚을 수 있도록 하겠습니다.

2023년 1월

소순형 드림